Geophysical Journal International

Geophys. J. Int. (2024) **239,** 591–620
Advance Access publication 2024 August 14
GJI Seismology

https://doi.org/10.1093/gji/ggae285

Examining the influence of 2.5-D ultra-low velocity zone morphology on ScP waveforms and estimated elastic parameters

Surya Pachhai [1], Michael S. Thorne [1] and Sebastian Rost [2]

[1] *Department of Geology and Geophysics, University of Utah,* 115 *S* 1460 *E* #383, *Salt Lake City, UT,* 84112, *USA. E-mail: surya.pachhai@utah.edu*
[2] *Institute of Geophysics and Tectonics, School of Earth and Environment, University of Leeds, Leeds LS*2 9*JT, UK*

Accepted 2024 August 13. Received 2024 August 13; in original form 2024 March 13

SUMMARY

Ultra-low velocity zones (ULVZs) have been identified as regions of extremely low velocity anomalies in the Earth's lowermost mantle using seismic observations from reflected, refracted and diffracted arrivals along the mantle side of the core–mantle boundary. Estimation of ULVZ geometrical (i.e. shape and size) and elastic (i.e. velocity and density) parameters with uncertainties is crucial in understanding the role of ULVZs in the ongoing dynamic processes within the Earth's mantle; however, these parameters are still poorly known due to uncertainties and tradeoffs of the seismically resolved ULVZ geometries and elastic parameters. Computation of synthetic waveforms for 2-D and 3-D ULVZs shapes is currently computationally feasible, but past studies utilize higher dimensional waveform modelling of mostly only low-frequency diffracted waves. Most studies focusing on high-frequency core-reflected waveforms (e.g. ScP) still use 1-D modelling approaches to determine ULVZ properties. This approach might lead to wrong results if the imaged structures have inherently 3-D geometries. This study investigates high-frequency synthetic ScP waveforms for various 2.5-D ULVZ geometries showing that additional seismic arrivals are generated even when the ScP geometrical ray path does not directly strike the location of the ULVZ. The largest amplitude additional phases in the 2.5-D models are post-cursor arrivals that are generated at the edges of the finite-length ULVZs. These newly identified ScP post-cursors can arrive within the ScsP post-cursor time window traditionally analysed in 1-D ULVZ studies. These post-cursors might then be misidentified or constructively/destructively interfere with the ScsP post-cursor, leading to incorrect estimation of ULVZ parameters. In this study we investigate the bias introduced by the 2.5-D morphologies on the 1-D estimated ULVZ elastic properties in a Bayesian waveform inversion scheme. We further expand the Bayesian method by including the data noise covariance matrix in the inversion and compare it to an autoregressive noise model that was utilized in previous studies. From the application to the observed ScP data, we find that the new approach converges faster, particularly for the inversion of data from multiple events, and the new algorithm retrieves ULVZ parameters with more realistic uncertainties. The inversion of 2.5-D synthetic ScP waveforms suggests that the retrieved ULVZ parameters can be misleading with unrealistically high confidence if we do not consider the data noise covariance matrix in the inversion. Our new approach can also retrieve the shape of a multidimensional Gaussian ULVZ if its length is 12° or longer in the great circle arc direction. However, 2.5-D synthetic waveforms show additional waveform complexity which can constructively interfere with the ScP wavefield. Hence, in many cases the estimation of ULVZ properties using 1-D forward modelling can provide incorrect ULVZ parameters. Hence previous ULVZ modelling efforts using 1-D parameter estimation methods may be incorrect.

Key words: Bayesian inference; Body waves; Computational seismology; Core-mantle boundary; Waveform inversion.

1 INTRODUCTION

Ultra-low velocity zones (ULVZs) are thin structures, with extremely low seismic velocities, sitting on the top of the core–mantle boundary (CMB). ULVZ lateral extent is reported as short as ∼10′s of km to as long as more than 1000 km on the CMB (e.g. Rost *et al.* 2005; Thorne *et al.* 2013). What defines these structures is the reported strong decrease in shear (*S*)-wave velocity (δV_S) of up to 50 per cent (e.g. Havens & Revenaugh 2001; Rondenay & Fischer 2003), a strong reduction in compressional (*P*)-wave velocity (δV_P) up to 25 per cent (e.g. Thybo *et al.* 2003), and an increase in density ($\delta \rho$) up to 20 per cent (e.g. Koper & Pyle 2004). Although ULVZs are identified as relatively small structures in the lowermost mantle, they can play a crucial role in ongoing processes in the Earth's interior. For example, multiple studies have suggested that ULVZs might represent the root of upwelling mantle plumes (e.g. Rost *et al.* 2005; Cottaar & Romanowicz 2012; Jenkins *et al.* 2021; Krier *et al.* 2021; Cottaar *et al.* 2022 and Yuan & Romanowicz 2017). This scenario has traditionally invoked partial melting to explain ULVZ occurrence (e.g. Williams & Garnero 1996; Williams *et al.* 1998), however, multiple recent studies have shown that increasing iron content in lower mantle minerals is also a viable method to generate ULVZ properties (e.g. Mao *et al.* 2006; Wicks *et al.* 2010). If ULVZs are compositional heterogeneities, geodynamic modelling efforts have demonstrated that ULVZs are one of the most dynamically active features in the lowermost mantle and may be actively moving across the CMB (e.g. McNamara *et al.* 2010; McNamara 2019). If large low velocity provinces (LLVPs) signify compositional heterogeneities, ULVZs should accumulate along their boundaries (e.g. McNamara *et al.* 2010; Li *et al.* 2017) which may in turn be linked to the locations of plume upwellings (e.g. Thorne & Garnero 2004). Alternatively, even if the LLVPs do not represent thermochemical structures, ULVZs should ultimately converge and congregate at locations of active mantle upwelling (e.g. Li *et al.* 2016).

Determining the origin of ULVZ material has remained speculative with multiple viable scenarios being proposed. For example, ULVZs may arise through ongoing processes such as melting of Mid-Ocean Ridge Basalt (MORB) material in down-going slabs (Andrault *et al.* 2014) or are being actively generated through core–mantle reactions (e.g. Kanda & Stevenson 2006). But they could also be extremely long-lived features and represent the remnants of a basal magma ocean that formed after the differentiation of our planet (Labrosse *et al.* 2007; Pachhai *et al.* 2022). Discriminating between these scenarios is not possible at this time due to the uncertainties and tradeoffs of the seismically derived ULVZ parameters, uncertainties in the mineral physical properties of lowermost mantle materials and the small-scale structure of ULVZ making geodynamical and seismic modelling difficult. A recent global survey of ULVZ locations (Thorne *et al.* 2020; Thorne *et al.* 2021) has demonstrated that ULVZs exist in all major provinces of the lowermost mantle, including LLVP regions and the circum-Pacific. Thus, the origin of ULVZ features may not necessarily arise from just one mechanism, or ULVZs in different locations are manifestations of a single phenomenon at different stages of their life cycle.

ULVZs were first discovered three decades ago (Garnero *et al.* 1993) and have subsequently been studied using a wide variety of seismic observations. The earliest studies solely made inferences on δV_P, which were determined to be ∼-5 to -10 per cent, with respect to the PREM model (Dziewonski & Anderson 1981), concentrated in zones that were likely a few 10′s of km thick (Garnero *et al.* 1993; Garnero & Helmberger 1995; Mori & Helmberger 1995; Garnero & Helmberger 1996). The first suggestion that the low velocities encountered in ULVZs may be composed of partial melt was provided in Garnero & Helmberger (1996) and subsequently expounded upon in Williams & Garnero (1996) with the prediction of a ratio of 3:1 for δV_S to δV_P, meaning that δV_S could be as large as -15 to -30 per cent. Evidence for such large *S*-wave velocity drops was first presented in Revenaugh & Meyer (1997). However, from the onset it was recognized that strong tradeoffs in the model space make determination of elastic parameters uncertain (Garnero & Helmberger 1998). Approximately 30 per cent of published ULVZ studies to date have utilized diffracted waveforms such as those originally used to infer ULVZ presence (e.g. P_{diff}, S_{diff}, $SP_{diff}KS$, $SKP_{diff}S$ and $PKKP_{diff}$) (see Yu & Garnero 2018 for a review). But more than half of all ULVZ studies conducted have used core-reflected waveforms (PcP and ScP). One of the most alluring aspects of using these phases is that, if found, pre- and post-cursor arrivals offer the potential of constraining all ULVZ elastic parameters (see e.g. Mori & Helmberger 1995; Garnero & Vidale 1999) and potential internal structure (Rondenay & Fischer 2003; Thybo *et al.* 2003; Idehara 2011; Pachhai *et al.* 2022). In contrast, diffracted phases such as $SP_{diff}KS/SKP_{diff}S$ or Sdiff, are relatively insensitive to such internal layering which makes studying the reflected phases attractive.

In order to infer ULVZ properties, the earliest studies utilized 1-D waveform modelling techniques such as generalized ray theory and the reflectivity technique, regardless of seismic phases used (e.g. Mori & Helmberger 1995; Garnero & Helmberger 1996; Reasoner & Revenaugh 2000). However, modelling seismic waveforms for the long period $SP_{diff}KS$ seismic phase in 2-D models began as early as the late 1990′s using hybrid techniques (Helmberger *et al.* 1998; Wen & Helmberger 1998). The 2-D and 2.5-D modelling of $SP_{diff}KS$ waveforms for ULVZs became widespread in the last decade (e.g. Rondenay *et al.* 2010; Jensen *et al.* 2013; Thorne *et al.* 2013; Vanacore *et al.* 2016) and 3-D modelling has just recently become practical (Krier *et al.* 2021; Thorne *et al.* 2021). Modelling of long period S_{diff} waveforms has also extensively utilized 2-D or 3-D waveform modelling techniques (e.g. Cottaar & Romanowicz 2012; Yuan & Romanowicz 2017; Cottaar *et al.* 2022). Sun *et al.* (2019) present modelling of ScS waveforms at higher frequency for various shapes (triangle, boxcar and Gaussian) of ULVZ. But for high frequency arrivals such as ScP and PcP concurrent modelling still existed only in the 1-D model space (e.g. Rost *et al.* 2010; Idehara 2011; Thorne *et al.* 2021; Pachhai *et al.* 2022, 2023). The first 2-D modelling of ScP, albeit for longer period waveforms, was explored in Brown *et al.* (2015). But forward waveform modelling capabilities now make it possible to model these waveforms at high frequency using 2-D or 3-D techniques. A recent paper (Pachhai *et al.* 2023) also laid the groundwork for modelling ScP at high frequencies for 2.5-D model geometries and presented an initial analysis of 2.5-D seismic waveforms. In the presence of a 2-D boxcar ULVZ additional arrivals due to likely diffraction at the edge boundaries exists. The amplitudes and arrival times of these additional phases depend on the ScP bounce point and the edge location of the ULVZ. We present more details of these arrivals in this paper.

The importance of considering higher dimensional ULVZ morphology is implicit as additional post-cursor arrivals may be generated, even if the ScP wave does not directly strike the ULVZ along the geometric ray path. Several key features of the seismic waveforms shown in Pachhai *et al.* (2023) make additional investigation

important, especially when considering characteristics of observed ULVZ signatures.

Fig. 1 summarizes where ULVZs have and have not been detected using ScP in a relatively small region beneath the Coral Sea. These lateral variations of detected/undetected ULVZ locations at the CMB are due to the ScP observations that show a wide variation of ScP waveforms sampling within a few tens of kilometres at the CMB. Some events show waveforms without complexity (i.e. lack of both pre- and post-cursor signal) while others show complex ScP waveforms, i.e. waveforms with precursors and multiple post-cursors. As can be seen in Fig. 1(b), there is a high degree of overlap between the regions showing and not showing ULVZ signature (fig. 1b; Rost & Revenaugh 2003; Rost *et al.* 2005, 2006; Idehara 2011; Brown *et al.* 2015). Many of these seemingly conflicting observations could be explained by higher dimensional ULVZ structure that has not previously been considered. For example, as shown in Pachhai *et al.* (2023), we see that ScP post-cursors (but no precursors) may exist when the ScP geometric ray does not strike the ULVZ due to the finite frequency of the seismic wave. Also, strong constructive/destructive interference effects between ScsP post-cursor and additional post-cursor arrivals may exist for 2-D/3-D ULVZ, making the ScsP post-cursor increase dramatically in amplitude or even cease to be observable. Furthermore, if ULVZs contain sharp edges then multipath arrivals could complicate the picture even further. These highly variable ScP characteristics have not only been observed beneath the east of Australia (e.g. Pachhai *et al.* 2023) but also beneath other areas such as the Philippines (e.g. Idehara 2011). In some cases, ScP post-cursors have been observed without any accompanying precursors (e.g. Rost & Revenaugh 2003; Rost *et al.* 2005).

In this paper, we explore the nature of ScP arrivals generated by 2.5-D ULVZ model geometries. We first compute a set of synthetics for a variety of ULVZ morphologies, identifying the new arrivals observed in the synthetic wavefield. We next use these synthetics to invert for ULVZ structure using state-of-the-art Bayesian waveform inversion methods (Pachhai *et al.* 2014, 2015, 2023). Here we further enhance our Bayesian inversion method to assess under what circumstances the 1-D inversion results may be applicable and how 2.5-D ULVZ structure may bias those results. In our past Bayesian inversion of ScP waveforms, we parametrized the data noise covariance matrix by two parameters in an autoregressive model (width of the noise correlation represented by AR1 coefficient and the standard deviation of the noise). In general, a higher value of the AR1 coefficient is linked to the wider band correlation matrix. However, in this study we consider the full data noise covariance matrix in the inversion without any approximation. Past ULVZ studies (e.g. Pachhai *et al.* 2014, 2015) did not consider this approach as parametrization of noise covariance matrix using two parameters is more efficient than computing the covariance matrix, particularly when we consider a single event in the inversion. We also examine the effects of inverting for ULVZ parameters, using the most state-of-the-art 1-D inversion scheme, to gain a first-order estimate as to how much previous study results may have been affected by waveform effect due to higher dimensional ULVZ properties. Our synthetic experiments suggest that the inclusion of the noise covariance matrix in the likelihood function retrieves more meaningful ULVZ properties in comparison to those obtained using the AR1 coefficient in previous studies, but that 2.5-D ULVZ morphology adds considerable differences to the ScP wavefield making recovery of true ULVZ parameters challenging.

2 SYNTHETIC DATA

In nearly all previous ScP studies, forward modelling waveforms have been computed using 1-D modelling, assuming ULVZs are flat layered structure (e.g. Garnero & Vidale 1999; Reasoner & Revenaugh 2000; Rost & Revenaugh 2003; Idehara 2011; Pachhai *et al.* 2022). This approximation has been used to predict and interpret the pre- and post-cursors of ScP waves in terms of ULVZ parameters. However, the literature is virtually absent on 2-D or 3-D effects on the seismic waveforms, particularly for high frequency wavefields such as ScP that has dominant period of 1 s. Here we explore the effect of 2.5-D ULVZ models on the ScP wavefield by computing synthetic seismograms using the PSVaxi technique (e.g. Jahnke 2009; Jensen *et al.* 2013; Thorne *et al.* 2013). The PSVaxi technique is a finite difference method for solving the seismic wave equation. Model geometries are input on a 2-D grid, and the grid is virtually rotated around a line passing through the source and the centre of the Earth. This provides correct 3-D geometrical spreading effects, albeit for 2-D input models. Computation of full 3-D synthetic seismograms is now possible (Leng *et al.* 2020), but that does not allow us to compute synthetics for many models. The PSVaxi applied here is computationally efficient than the other existing methods such as 3-D spectral-element method (SEM; Komatitsch & Tromp 2002), axisymmetric SEM3D (Leng *et al.* 2016) and allows us to compute synthetics for various ULVZ shape and size in a reasonable time.

We calculate synthetic seismograms using three types of 2.5-D model geometries: (1) Boxcar, (2) Tukey window (hereinafter referred to as just Tukey) and (3) Gaussian shaped ULVZs. In contrast to 1-D ULVZ properties, 2.5-D ULVZs are defined by geometric and elastic parameters. The geometric parameters are defined by shape with sharp or smoothed edges, length and its edge locations. Similar to 1-D ULVZs, the elastic parameters are defined by a percentage decrease in *S*-wave velocity (δV_S), a percentage decrease in *P*-wave velocity (δV_P) and a percentage increase in density ($\delta\rho$) with respect to a 1-D Earth model. Example ULVZ shapes and defining parameters are shown in Fig. 2(a). In this paper, all synthetic seismograms are computed for a dominant period of 2.5 s and source depth of 500 km, and we only show synthetics at an epicentral distance of 40° which has no other contaminating arrivals. Although it is computationally feasible to compute synthetics at shorter periods (e.g. 1 s) this dramatically increases the computational resources required and would significantly reduce the number of models we can explore.

2.1 2.5-D synthetic ScP waveforms for Boxcar ULVZ

The geometric parameters, for a boxcar ULVZ, are defined by a constant height ($h_{\max}$) within the box and zero outside the box (eq. 1).

$$h(\theta) = \begin{cases} 0, & \theta \ \langle\, l_1 \text{ or } \theta \,\rangle \ l_2 \\ h_{\max}, & l_2 \ \geq \ \theta \ \geq \ l_1 \end{cases}, \tag{1}$$

where l_1 is the leading edge of the ULVZ and l_2 is the terminating edge of the boxcar ULVZ (Fig. 2). For boxcar shaped models we define the length of the ULVZ in the great-circle path as l. Therefore, distance of the terminating edge of ULVZ from the source becomes $l_2 = l_1 + l$.

The bounce point on the CMB for an ScP arrival at 40° for a 500 km source depth occurs at an angular distance of 11.1° away from the source. This means that if a boxcar ULVZ is located with its leading edge $l_1 = 11.1°$, the ScP bounce point on the CMB

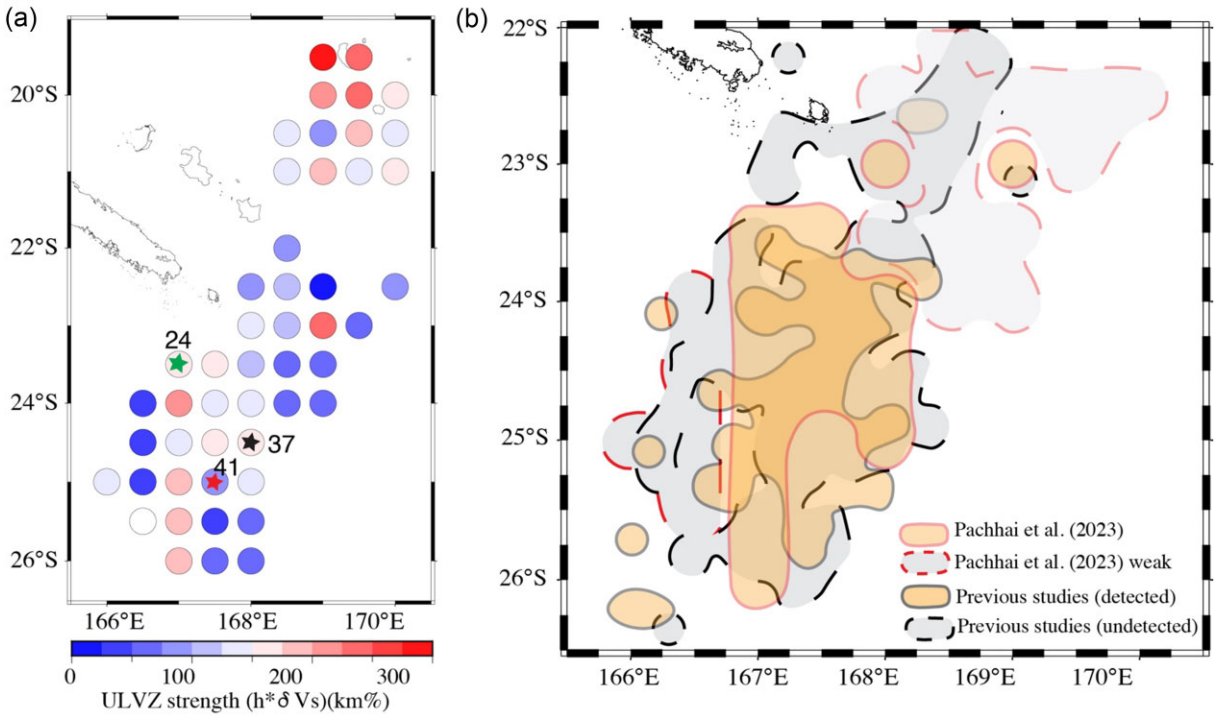

Figure 1. (a) ULVZ strength beneath the Coral Sea estimated by Pachhai *et al.* (2023). Stars with different colours represent the bins that are analysed in this study using noise covariance matrix in the inversion to compare with the results from Pachhai *et al.* (2023). (b) Strong and weak ULVZs detected in Pachhai *et al.* (2023) overlayed on previous studies reported detected (Rost & Revenaugh 2001, 2003; Rost *et al.* 2005, 2006; Idehara 2011; Brown *et al.* 2015; Pachhai *et al.* 2022), and undetected (Rost & Revenaugh 2003; Rost *et al.* 2005, 2006) ULVZ using ScP data.

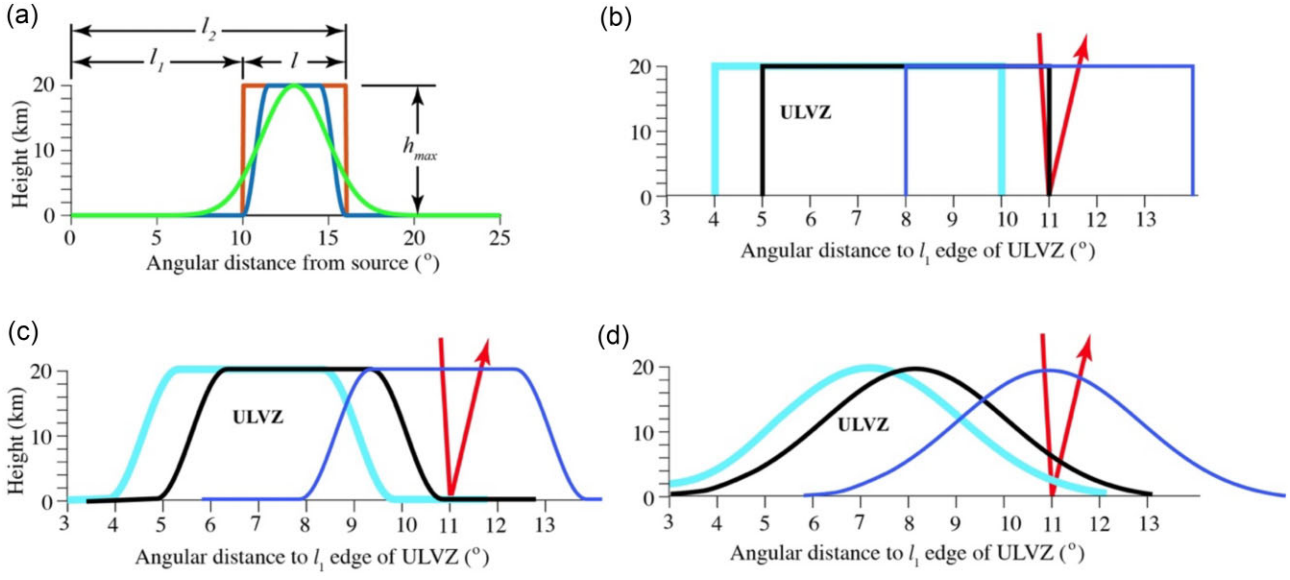

Figure 2. (a) Geometry of 2.5-D ULVZ models. Models are for boxcar (red), Tukey window (blue) or Gaussian (green) shaped ULVZ. The parameters are: l—the length of the ULVZ in the great circle arc distance, l_1–the angular distance to the leading edge of the ULVZ from a line passing through the source and the centre of the Earth and l_2—the angular distance to the trailing edge of the ULVZ. The maximum height of ULVZ is $h_{\max} = 20$ km, with edge $l_1 = 10°$ and length $l = 6°$. (b) Boxcar ULVZ geometry positioned at three different l_1 edge locations (4°—cyan, 5°—black and 8°—blue) relative to the source. Same as (b) but for the (c) Tukey and (d) Gaussian shape of ULVZ. ULVZ with $h_{\max} = 20$ km and $l = 6°$ are overlain for a ScP ray path for an epicentral distance of 40°. The x-axis shows the angular distance to the l_1 edge of the ULVZ. By changing the l_1 edge position, where the down going ScP ray interacts with the ULVZ changes.

would coincide with the ULVZ boundary. A depiction of where the ScP bounce point occurs with respect to ULVZ models explored in this study is shown in Fig. 2(b). This figure shows an example ULVZ with a length of 6°. For example, if $l_1 = 8°$ (depicted by a blue rectangle) then the ScP ray traverses approximately through the centre of the ULVZ which is depicted by the black ScP ray that has a bounce point shown corresponding to the $l_1 = 8°$ position. If $l_1 = 4°$ (depicted by a cyan rectangle), the ScP bounce point is

located on the far-side of the ULVZ (right-hand side of the ULVZ—cyan rectangle in Fig. 2b). If $l_1 = 5^\circ$ (black rectangle), the ScP bounce point would occur near the l_2 edge of the ULVZ.

The elastic parameter perturbations are fixed inside the boxcar and are set to zero outside the box. Fig. 3 shows synthetic seismograms for a boxcar ULVZ model with $h_{\max} = 25$ and 15 km, $\delta V_S = -20$ per cent, $\delta V_P = -10$ per cent, $\delta\rho = 5$ per cent with respect to the PREM model (Dziewonski & Anderson 1981), and $l = 6^\circ$ for a variety of leading-edge positions (l_1). At the bottom of the figure, the blue trace shows the PREM prediction, which consists of a single ScP arrival which we refer to as ScP$^{\text{PREM}}$ (Fig. 4 for ray path). The red trace shows the prediction for the 1-D ULVZ model. In the 1-D model, ScP delays as it traverses through the ULVZ, and we refer to this arrival as ScP$^{\text{ULVZ}}$ to distinguish it from the earlier arriving ScP$^{\text{PREM}}$ (Fig. 4 for ray path). In addition, we see the ScsP post-cursor and the SPcP pre-cursor for 1-D ULVZ model (Fig. 4 for ray path). The SdP precursor (Fig. 4 for ray path) amplitude is too low to be observed for this model. The black traces in Fig. 3 show predictions for the 2.5-D models for 25 different l_1 positions. The grey shaded region outlines the predictions where the 1-D ray prediction for ScP would have its bounce point inside of the ULVZ (i.e. between $l_1 = 5.1^\circ$ and $l_1 = 11.1^\circ$). The waveforms for the 2.5-D synthetics look significantly different than that for the 1-D models as we explain below.

For models where the ScP bounce point does not occur within the ULVZ (e.g. roughly from, $2^\circ \leq l_1 \leq 4^\circ$ and $12^\circ \leq l_1 \leq 14^\circ$), we observe an ScP arrival that is coincident in time with ScP$^{\text{PREM}}$. Similarly, for models where the ScP bounce point is within the ULVZ (e.g. $6^\circ \leq l_1 \leq 10^\circ$), we observe an ScP arrival that is coincident in time with ScP$^{\text{ULVZ}}$. Near the ULVZ boundaries (e.g. $l_1 \cong 5.1^\circ$ and $l_1 \cong 11.1^\circ$, we observe multipathing of the ScP arrival and two ScP arrivals exist with ScP$^{\text{PREM}}$ and ScP$^{\text{ULVZ}}$ arrival times. The SPcP pre-cursor is most conspicuously observed when the ScP bounce point occurs within the ULVZ. However, its timing does not always coincide with the 1-D prediction, and it also exists for ULVZ models where the ScP bounce point is within $\sim 1^\circ$ of the ULVZ boundary. The ScsP post-cursor is also most conspicuous when the ScP bounce point occurs within the ULVZ and in this case the timing of this post-cursor agrees well with the 1-D prediction. Yet an apparent ScsP post-cursor appears to exist for all 2.5-D models shown in this figure, although its amplitude likely drops below the noise level as the ScP bounce point gets further away from the ULVZ. Nonetheless, the amplitude of the ScsP post-cursor for bounce points within the ULVZ is heavily modulated by interference from two new arrivals that we refer to here as Sl_1P and Sl_2P. These new arrivals are predicted in 2-D ULVZ models and do not exist in the 1-D scenario. These are named as such because they are generated at the l_1 and l_2 boundaries (see Fig. 4) of the ULVZ as described below.

In all the synthetic tests we have performed, the Sl_2P arrival has the largest amplitude and may be the more important of these two new post-cursors. To further understand where this arrival originates, we conducted parameter sensitivity tests and viewed animations of the 2.5-D ScP wavefield in the vicinity of a ULVZ provided as supplements to Thorne *et al.* (2021). Sensitivity tests for the Sl_2P arrival are shown in Fig. 5. Here we use the same model as shown in Fig. 3, but we focus on models near the $l_1 = 13^\circ$ edge where the Sl_2P arrival is well separated from other arrivals. The following observations are obtained from the sensitivity analysis.

(1) The onset of Sl_2P arrival does not change if we change the δV_S (Fig. 5a), change the δV_P (Fig. 5b) or the l_1 position (Fig. 5d). In the latter test for l_1 position, we vary the length of the ULVZ such that the l_2 position always remains the same.

(2) The onset of Sl_2P arrival varies slightly if we change the ULVZ height (Fig. 5c), specifically, increasing the ULVZ thickness also increases the Sl_2P arrival time.

(3) The most significant variation in arrival time occurs if we vary the l_2 position (Fig. 5e). The farther the l_2 edge is from the source the more delayed the Sl_2P arrival is.

(4) The Sl_2P amplitudes are unaffected by *P*-wave velocity (Fig. 5b), l_1 edge location (Fig. 5d) and l_2 edge location (Fig. 5e).

(5) The amplitude of Sl_2P is significantly altered by ULVZ height (larger ULVZ heights give a larger amplitude arrival—Fig. 5c) and with changes in δV_S (larger reductions in *S*-wave velocity give larger amplitude arrivals—Fig. 5a).

From these analyses and examination of animations of the seismic wavefield, we conclude that this arrival occurs when the downgoing *S*-wave energy interacts with the l_2 boundary of the ULVZ. The traveltime is consistent in ray tracing with a downgoing *S* wave that goes to the upper-right hand corner of the ULVZ at the l_2 boundary, traverses down the right-hand edge of the ULVZ and then converts to a *P* wave at the CMB. The ray path for this arrival is shown in Fig. 4 and appears to be a surface diffraction along the right-hand boundary of the ULVZ, e.g. Schwarz (2019). This arrival is not an edge diffraction from the ULVZ corner as can be seen by the dependence on traveltime with ULVZ thickness (see Fig. 4 for ray path). If the arrival were an edge diffraction, a thicker ULVZ would result in an earlier Sl_2P arrival. However, what is observed is exactly opposite of that, in that a thicker ULVZ results in a more delayed Sl_2P arrival as the actual ray path travels down along the boundary of the ULVZ before converting to a *P* wave.

Similar to the sensitivity test shown above, we also conducted a sensitivity test for the Sl_1P arrival, which are shown in Fig. 6. Again, we use the same model as shown in Fig. 3, but we focus on models near the $l_1 = 4.5^\circ$ edge. This sensitivity analysis reveals the following observations.

(1) The onset of Sl_1P arrival time is unaffected by *S*-wave velocity (Fig. 6a) and only minorly affected by ULVZ thickness (Fig. 6c). There appears to be a slight delay due to thickness, but in going from $h_{\max} = 15$ km to $h_{\max} = 35$ km, the Sl_1P arrival is only delayed by a few tenths of seconds.

(2) The arrival time of Sl_1P is affected by P-wave velocity. The larger the P-wave velocity decrease the more delayed Sl_1P becomes (Fig. 6b).

(3) The arrival time of Sl_1P is most strongly affected by l_1-edge position (Fig. 6e). The closer the l_1-edge is to the source, the more delayed Sl_1P is.

(4) The amplitude of Sl_1P is affected by *P*- and *S*-wave velocity (Figs 6a and b). The larger the *P*- or *S*-wave velocity decrease the larger the Sl_1P amplitude becomes. In addition, the Sl_1P amplitude increases as l_1-edge moves further away from the source (Fig. 6d).

The origin of the Sl_1P arrival is unclear. Ray tracing an edge diffracted arrival from the l_1-edge matches the traveltime moveout of Sl_1P but does not perfectly match the absolute arrival time. There exists a small dependence on *P*-wave velocity and ULVZ thickness in the arrival time (Fig. 6), that suggests the arrival may convert from S-to-P on the outside of the ULVZ and travel a small distance inside the ULVZ, perhaps refracting as a *P* wave inside the ULVZ (see Fig. 4 for ray path). The exact ray path for this arrival is unclear, but it is most strongly related to the top left-hand position of the

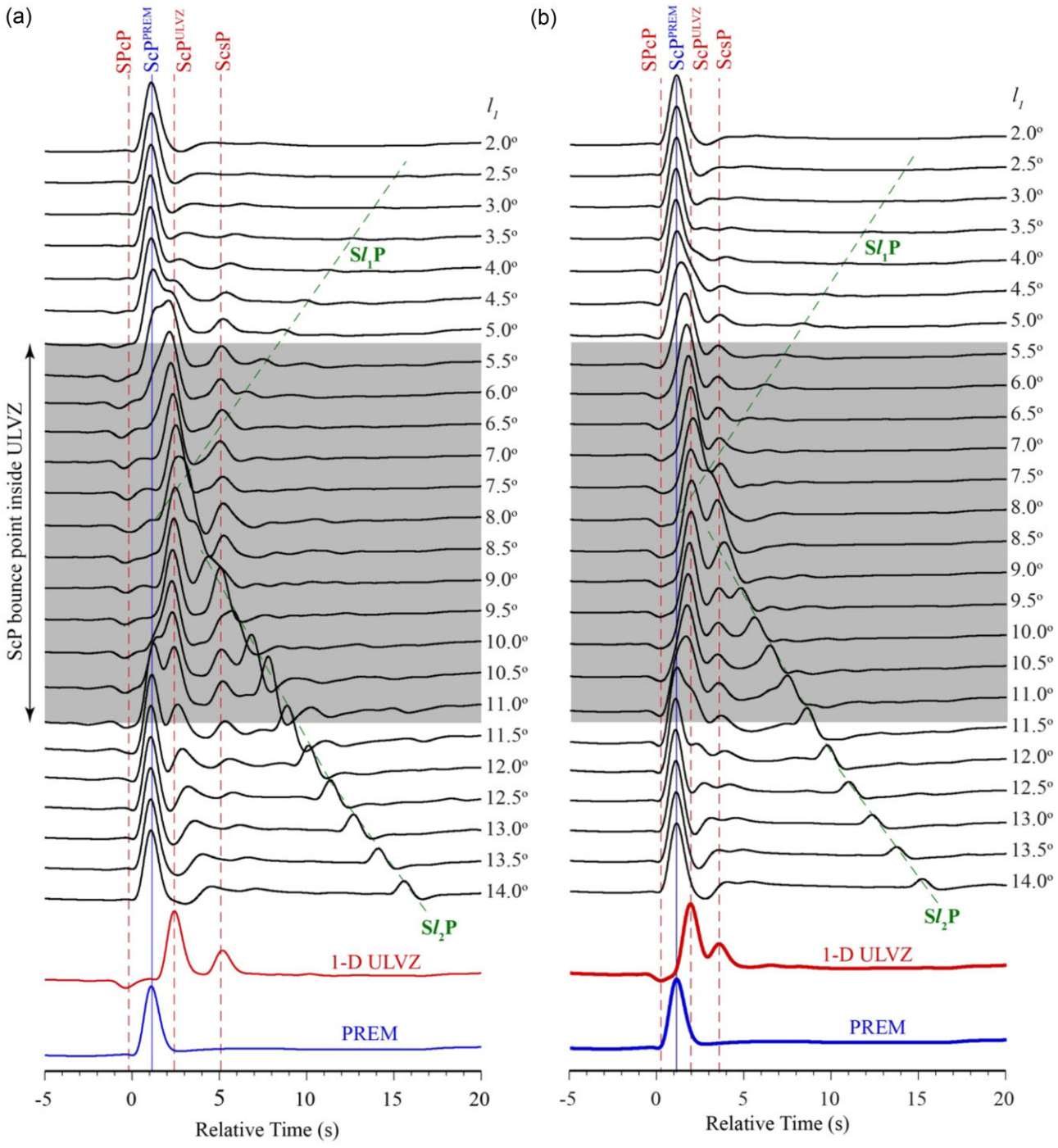

Figure 3. (a) Synthetic seismograms for PREM (blue) and a 1-D ULVZ model (red) with δV_S = -20 per cent, δV_P = -10 per cent, $\delta\rho$ = +5 per cent and h = 25 km. The 2.5-D boxcar ULVZ synthetics (black) are shown for models with the same elastic parameters as the 1-D model, a length $l = 6^\circ$, and edge positions l_1 from 2.0° to 14.0°. The 1-D ScP ray path directly hits the ULVZ for l_1 positions between 5.1° and 11.1°, which is indicated by the grey shaded area. Red dashed lines indicate the arrival times for standard ULVZ phases (SPcP, ScP^{ULVZ} and ScsP) associated with 1-D ULVZ models. Green dashed lines show approximate arrival for edges (Sl_1P and Sl_2P) of 2.5-D ULVZ. The arrival time of ScP phase in PREM is indicated by the blue line (ScP^{PREM}). All seismograms are vertical component displacement aligned on the PREM predicted ScP arrival time and normalized to unity. (b) Same as (a), except the ULVZ model has a reduced thickness of h = 15 km.

ULVZ. In Fig. 4, we draw the ray path to the left-hand boundary of the ULVZ and back up from there, but we do not understand the details.

The example ULVZ model with a thickness of h_{max} = 25 km shown in Fig. 3 serves as an excellent example to describe the seismic arrivals observable in 2.5-D models. This example clearly shows the multipathed ScP arrivals. However, ULVZs encountered within the Earth may not have such large thicknesses, and likely do not have boxcar shapes. This will result in waveforms that look slightly different than what we observe in Fig. 3. For example, Fig. 7 shows synthetic predictions for a thinner ULVZ model (h_{max} = 15 km) but for Tukey and Gaussian shapes. The predictions for this model

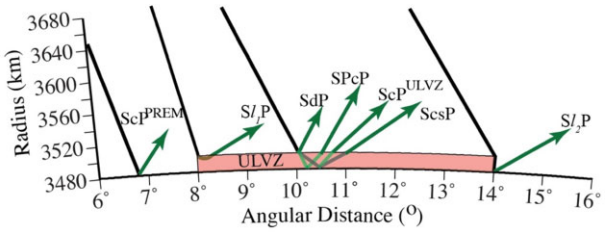

Figure 4. Ray paths for Sl_1P, ScP, Sl_2P and other converted phases (SdP, SPcP, ScP^{ULVZ} and ScsP present in the case of 1-D structure as well) due to a ULVZ at an epicentral distance of 40°. The ray paths are shown for a zoomed in region near the core–mantle boundary for a 20-km thick ULVZ with a length of $l = 6°$. The *S*-wave portion of the ray path is drawn in black and the *P*-wave portion of the ray path is drawn in green.

are similar to that shown in Fig. 3, except instead of a clear separation of the ScP^{PREM} and ScP^{ULVZ} multipathed waveforms these arrivals are not well-separated. Instead, we observe what appears to be a broadened ScP pulse when the ScP bounce point is near to the ULVZ boundaries due to the reduced time separation between the two multipathed arrivals. Otherwise, all the general characteristics of the thicker boxcar ULVZ model are retained, including the existence of the Sl_1P and Sl_2P arrivals. We note that in some cases (e.g. $l_1 \geq 9°$) that the Sl_2P arrival is predicted to have a larger amplitude than the ScsP post-cursor.

2.2 2.5-D synthetic waveforms for Tukey ULVZ

In the case of a Tukey shaped ULVZ, the ULVZ elastic parameter perturbations are set to zero outside the edges and are constant within the ULVZ. The ULVZ height changes as a function of distance from the source location (θ) given by

$$h(\theta) = \begin{cases} 0 & [\theta \langle l_1 \text{ or } \theta \rangle l_2] \\ 1 & [\theta > cond1 \text{ and } \theta < cond2] \\ \frac{h_{\max}}{2}\left(1+\cos\left(\pi\left(\frac{2(\theta-l_1)}{\beta l}-1\right)\right)\right) & [\theta \leq cond_1 \text{ and } \theta > l_1\ ] \\ \frac{h_{\max}}{2}\left(1+\cos\left(\pi\left(\frac{2(\theta-l_1)}{\beta l}-\frac{2}{\beta}-1\right)\right)\right) & [\theta \geq cond_2 \text{ and } \theta \leq cond_1\ ] \end{cases}, \tag{2}$$

where $\beta = 0.5$, $cond_1 = l_1 + \frac{\beta l}{2}$ and $cond_2 = l_1 + l(1 - \frac{\beta}{2})$. In contrast to boxcar ULVZ, the leading and terminating edge have symmetrical smoothing defined by last two expressions in eq. (2). An example of this ULVZ shape is shown in Figs 2(a) and (c), and 2.5-D synthetic waveforms for a Tukey shaped ULVZ with $h_{\max}$ = 15 km, δV_S = -20 per cent, δV_P = -10 per cent and $l = 6°$ are shown in Fig. 7(a). The waveforms look similar to those of the boxcar ULVZ models, except that the ScsP post-cursor becomes less prominent. There is also some broadening of the ScP pulse due to multipathing. Both Sl_1P and Sl_2P arrivals are visible, but their amplitude is weaker than in the case of boxcar ULVZ (Fig. 7a).

2.3 2.5-D synthetic waveforms for Gaussian ULVZ

In the case of Gaussian shape of ULVZ, the ULVZ elastic parameter parameters are set to zero outside the edges and are fixed within the ULVZ. The ULVZ height increases as a function of distance from the left edge and reaches its maximum at the centre of the ULVZ length, then decreases symmetrically until its height reaches to zero at the terminating edge of the ULVZ as defined in eq. (3).

$$h(\theta) = h_{\max} e^{-\frac{1}{2}\left(\frac{\alpha\pi}{l}\right)^2}, \tag{3}$$

where $\alpha = l_1 + \frac{l}{2} - \theta$. Example shape of Gaussian ULVZ is shown in Figs 2(a) and (d), and example waveforms for the same elastic parameters in the case of Gaussian ULVZ are shown in Fig. 7(b). In contrast to boxcar and Tukey ULVZ models, the ScsP post-cursor is invisible except in the case when ScP bounce near the centre of the Gaussian ULVZ (Fig. 7b). However, both Sl_1P and Sl_2P arrivals are observable and the amplitude of Sl_2P in the case of Gaussian ULVZ is similar to that of the Tukey ULVZ case, but Sl_1P is even weaker in the case of Gaussian shaped ULVZ in comparison to other models. Multipathing of ScP pulse also disappears in the case of the Gaussian model.

Examination of the 2.5-D synthetic seismograms shown above, reveal marked differences from the 1-D ULVZ model. In particular, we observe major amplitude variations in the ScsP post-cursor depending on model shape and due to constructive/destructive interference with the Sl_1P and Sl_2P arrivals. In addition, we see the additional Sl_1P and Sl_2P arrivals, that could be incorrectly interpreted as ScsP. In some cases, we also see the existence of a ScsP post-cursor even when the 1-D ScP ray path does not directly strike the ULVZ. These amplitude variations and potential misinterpretation of arrivals could significantly impact the interpretation of ULVZ thickness and *S*-wave velocity perturbations. It is possible that all previous efforts at determining ULVZ elastic parameters using ScP have been impacted by these higher dimensional waveform effects. In the next section we present a Bayesian inversion approach that considers the noise covariance matrix in the inversion to provide better estimates of the ULVZ elastic properties using 1-D forward modelling.

3 BAYESIAN INVERSION USING NOISE COVARIANCE MATRIX

In Bayesian inference, we consider posterior probability density (PPD) as a solution to the inverse problem, and PPD is defined by the probability of a model vector ($\boldsymbol{m}$) given the data vector ($\boldsymbol{d}$) (i.e. $p(\boldsymbol{m}|\boldsymbol{d})$). The PPD can be proportional to the product of the prior information and data information (incorporated through likelihood) through Bayes' theorem as:

$$p(\boldsymbol{m}|\boldsymbol{d}) \propto p(\boldsymbol{d}|\boldsymbol{m})\, p(\boldsymbol{m}), \tag{4}$$

where $p(\boldsymbol{d}|\boldsymbol{m})$ is the probability of data given the model parameter, also known as the likelihood, and $p(\boldsymbol{m})$ is the prior probability of model parameters. For a 1-D ULVZ model, the modelled ULVZ parameters are layer thickness (h), *P*-wave velocity (δVp), *S*-wave velocity (δVs) and density perturbations ($\delta\rho$).

3.1 Likelihood with covariance matrix and AR1 parametrization

In geophysical inversion the data are fixed, therefore, the likelihood function in eq. (4) is only a function of $\boldsymbol{m}$. In that case, the likelihood function can be represented as $L(\mathbf{m})$, which introduces data information to the inversion and is one of the most important components in Bayesian inversion. Likelihood is proportional to the negative exponential of the misfit function; therefore, it must be derived from an assumption about the statistical distribution of the data errors. The data errors are typically unknown but can be approximated by residual errors (i.e. the difference between the observed data and the synthetic prediction). These errors combine both measurement (e.g. errors due to noise in the recordings) and theory errors (e.g.

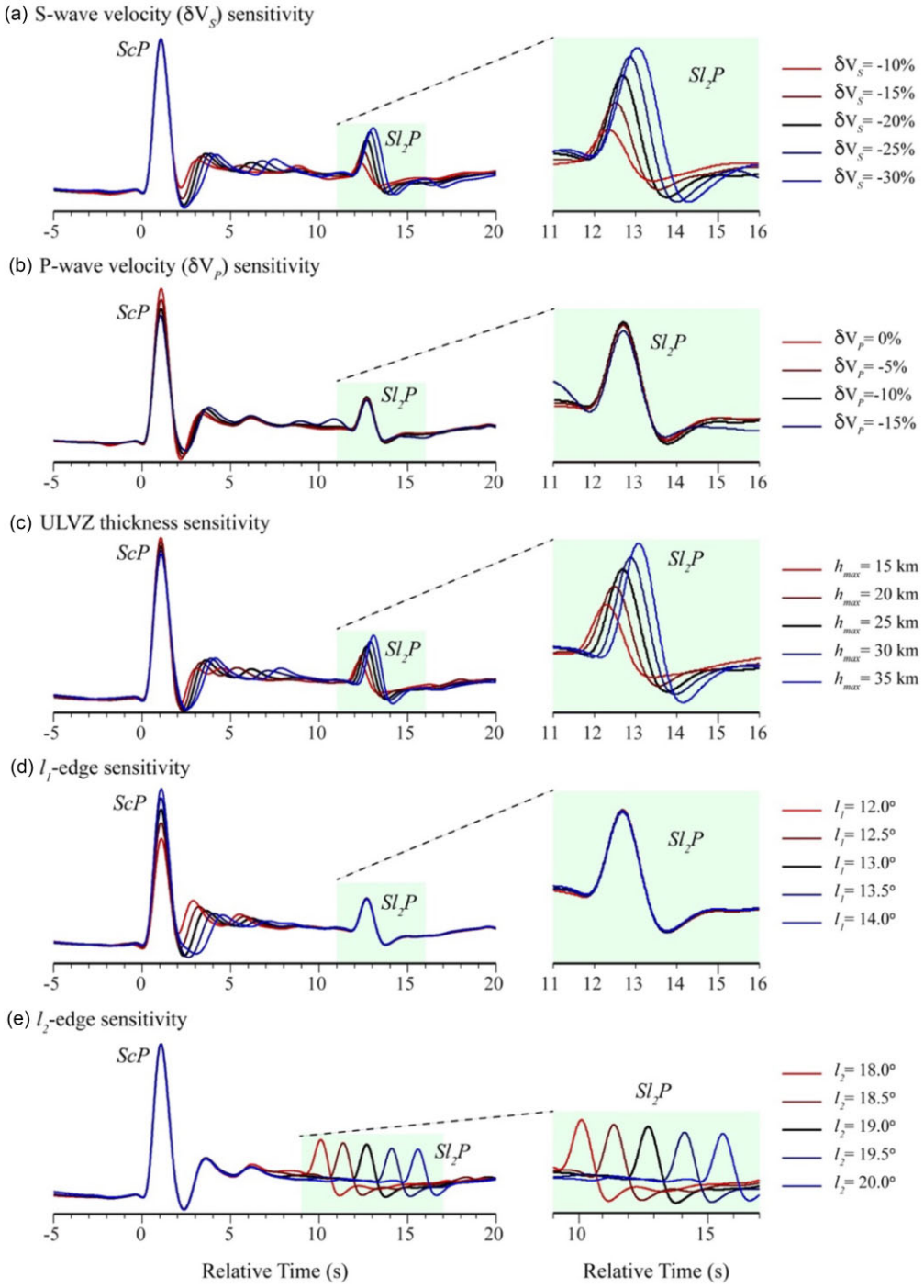

Figure 5. Sensitivity tests for Sl_2P arrival. In all panels the vertical component displacement seismograms are shown aligned on the PREM theoretical traveltimes for ScP. All seismograms are multiplied by a constant scaling factor so that absolute amplitudes are preserved. (a) Sensitivity to *S*-wave velocity perturbations. Synthetic seismograms are shown for a boxcar ULVZ model with δV_P = -10 per cent, $\delta\rho = +5$ per cent, $h_{\max} = 25$ km, $l = 6^\circ$, and $l_1 = 13.0^\circ$. In this case we changed *S*-wave velocity of the ULVZ from δV_S = -10 per cent (red trace) to -30 per cent (blue trace) in 5 per cent increments. (b) Sensitivity to *P*-wave velocity perturbations. Synthetic seismograms are shown for a boxcar ULVZ model with δV_S = -20 per cent, $\delta\rho = +5$ per cent, $h_{\max} = 25$ km, $l = 6^\circ$ and $l_1 = 13.0^\circ$. In this case we changed *P*-wave velocity of the ULVZ from $\delta V_P = 0$ per cent (red trace) to -15 per cent (blue trace) in 5 per cent increments. (c) Sensitivity to ULVZ thickness. Synthetic seismograms are shown for a boxcar ULVZ model with δV_S = -20 per cent, δV_P = -10 per cent, $\delta\rho = +5$ per cent, $l = 6^\circ$ and $l_1 = 13.0^\circ$. In this case we changed the thickness of the ULVZ from $h_{\max}$= 15 km (red trace) to 35 km (blue trace) in 5 km increments. (d) Sensitivity to l_1 edge position. Synthetic seismograms are shown for a boxcar ULVZ model with δV_S = -20 per cent, δV_P = -10 per cent, $\delta\rho = +5$ per cent and $h_{\max} = 25$ km. In these models l_2 position is held fixed at $l_2 = 19^\circ$. So, the models vary from $l_1 = 12^\circ$ and $l = 7^\circ$ (red trace) to $l_1 = 14^\circ$ and $l = 5^\circ$ (blue trace) in 0.5° increments, such that the only parameter that varies is the l_1 position. (e) Sensitivity to l_2 edge position. Synthetic seismograms are shown for a boxcar ULVZ model with δV_S = -20 per cent, δV_P = -10 per cent, $\delta\rho = +5$ per cent, $h_{\max} = 25$ km and $l_1 = 13^\circ$. The lengths (l) are changed such that we vary the l_2 position from 18.0° (red trace, $l = 5^\circ$) to 20.0° (blue trace, $l = 7^\circ$) in 0.5° increments. In each panel the green shaded region shows a zoomed in view of the Sl_2P arrival.

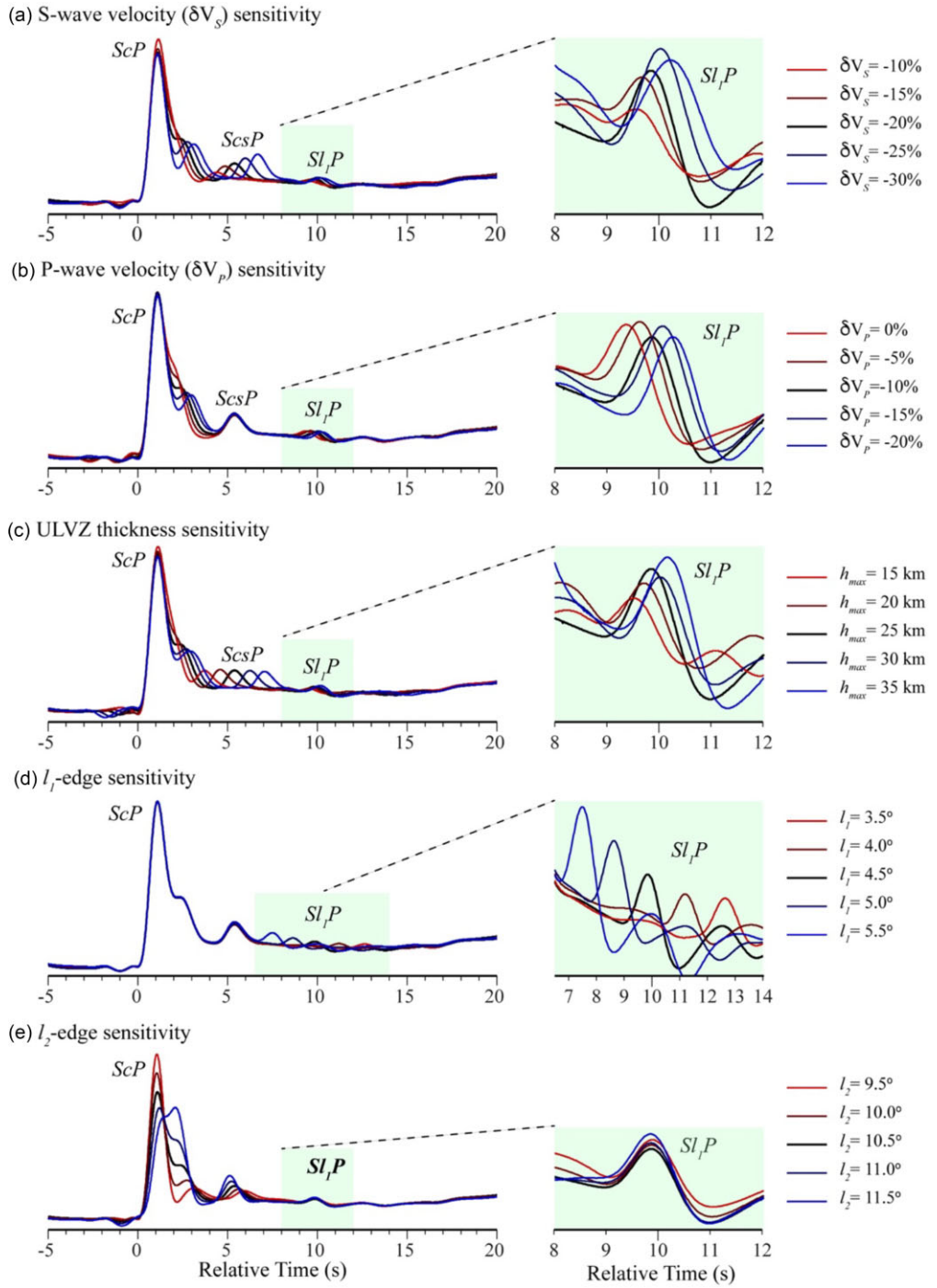

Figure 6. Sensitivity tests for Sl_1P arrival. In all panels the vertical component displacement seismograms are shown aligned on the PREM theoretical traveltimes for ScP. All seismograms are multiplied by a constant to preserve absolute amplitude information. (a) Sensitivity to *S*-wave velocity perturbations. Synthetic seismograms are shown for a boxcar ULVZ model with δV_P = -10 per cent, $\delta\rho = +5$ per cent, $h_{\max} = 25$ km, $l = 6^\circ$ and $l_1 = 4.5^\circ$. In this case we changed *S*-wave velocity of the ULVZ from δV_S = -10 per cent (red trace) to -30 per cent (blue trace) in 5 per cent increments. (b) Sensitivity to *P*-wave velocity perturbations. Synthetic seismograms are shown for a boxcar ULVZ model with δV_S = -20 per cent, $\delta\rho = +5$ per cent, $h_{\max} = 25$ km, $l = 6^\circ$ and $l_1 = 4.5^\circ$. In this case we changed *P*-wave velocity of the ULVZ from $\delta V_P = 0$ per cent (red trace) to -20 per cent (blue trace) in 5 per cent increments. (c) Sensitivity to ULVZ thickness. Synthetic seismograms are shown for a boxcar ULVZ model with δV_S = -20 per cent, δV_P = -10 per cent, $\delta\rho = +5$ per cent, $l = 6^\circ$ and $l_1 = 4.5^\circ$. In this case we changed the thickness of the ULVZ from $h_{\max} = 15$ km (red trace) to 35 km (blue trace) in 5 km increments. (d) Sensitivity to l_1 edge position. Synthetic seismograms are shown for a boxcar ULVZ model with δV_S = -20 per cent, δV_P = -10 per cent, $\delta\rho = +5$ per cent and $h_{\max} = 25$ km. In these models the l_2 position is held fixed at $l_2 = 10.5^\circ$. The models vary from $l_1 = 3.5^\circ$ and $l = 7^\circ$ (red trace) to $l_1 = 5.5^\circ$ and $l = 5^\circ$ (blue trace) in 0.5° increments, such that the only parameter that varies is the l_1 position. (e) Sensitivity to l_2 edge position. Synthetic seismograms are shown for a boxcar ULVZ model with δV_S = -20 per cent, δV_P = -10 per cent, $\delta\rho = +5$ per cent, $h_{\max} = 25$ km and $l_1 = 4.5^\circ$. The lengths (l) are changed such that we vary the l_2 position from 9.5° (red trace, $l = 5^\circ$) to 11.5° (blue trace, $l = 7^\circ$) in 0.5° increments. In each panel the green shaded region shows a zoomed in view of the Sl_2P arrival.

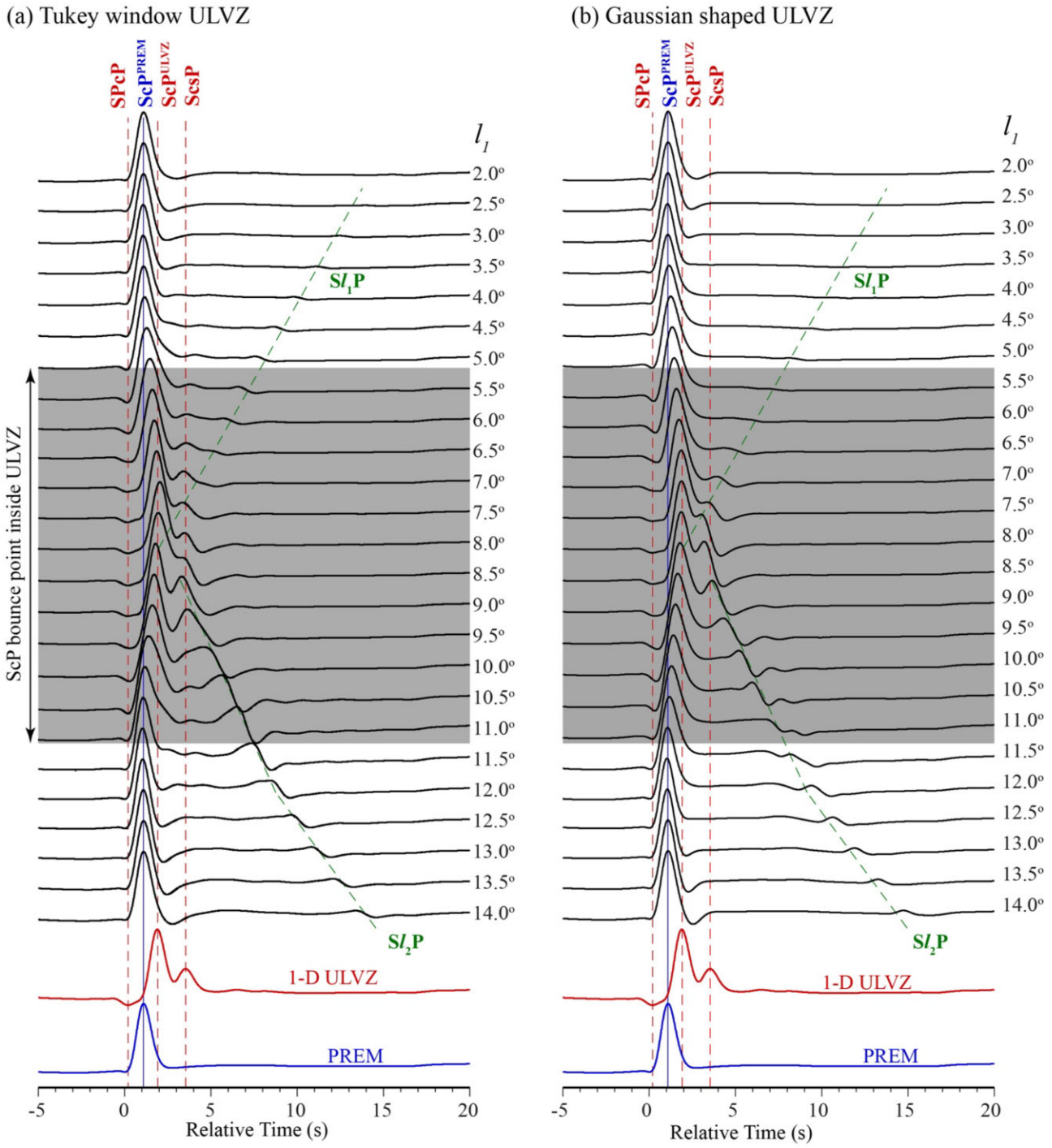

Figure 7. Same as in Fig. 3, except the ULVZ model has a shape of (a) a Tukey window, or (b) a Gaussian shape.

errors due to mathematical approximations in the forward calculations). Here, we assume a Gaussian form of data errors for ScP waveforms, therefore, the likelihood function becomes proportional to the negative exponential of the L2-norm misfit function. For data from nev number of events, the likelihood function can be written as

$$L(\boldsymbol{m}) = \prod_{i=1}^{\text{nev}} \frac{1}{|\boldsymbol{C}_{\boldsymbol{d}_i}|} \exp\left[-\left(\boldsymbol{d}_i^{\text{obs}} - \boldsymbol{d}_i(\boldsymbol{m})\right)^T \frac{1}{\boldsymbol{C}_{\boldsymbol{d}_i}} \left(\boldsymbol{d}_i^{\text{obs}} - \boldsymbol{d}_i(\boldsymbol{m})\right)\right], \quad (5)$$

where $\boldsymbol{C}_{\boldsymbol{d}_i}$ is the noise covariance matrix that incorporates both correlated and uncorrelated noise for data from i-th event, $|\boldsymbol{C}_{\boldsymbol{d}_i}|$ is the determinant of the noise covariance matrix, $\boldsymbol{d}_i^{\text{obs}}$ is the observed ScP waveforms from i-th event and $\boldsymbol{d}(\boldsymbol{m})$ is the theoretical prediction of ScP waveforms for models ($\boldsymbol{m}$). These predictions are obtained by convolving the source-time function (STF) with the Green's functions computed using the WKBJ method (Chapman & Orcutt 1985), i.e. $\boldsymbol{d}_i(\boldsymbol{m}) = \boldsymbol{G}_i(\boldsymbol{m}) * \text{STF}_i$. In the case of observed data, we used the stack of P waveforms at each array to obtain the empirical

STF for each event which is also referred as P wavelet or source wavelet.

In eq. (5), the noise covariance matrix can be approximated by the standard deviation of the residual errors if the noise is uncorrelated, i.e. $\boldsymbol{C}_{\boldsymbol{d}_i} = \sigma_i^2 \boldsymbol{I}$, where σ_i is the standard deviation of noise for i-th event. In that case, the likelihood function can be written as

$$L(\boldsymbol{m}) = \prod_{i=1}^{\text{nev}} \frac{1}{\left(2\pi\sigma_i^2\right)^{N_i/2}} \exp\left[-\frac{1}{2\sigma_i^2}\left|\boldsymbol{d}_i^{\text{obs}} - \boldsymbol{d}_i(\boldsymbol{m})\right|^2\right], \tag{6}$$

where N_i is the number of data points for i-th event.

However, noise can be strongly correlated due to several processing steps (e.g. filtering and stacking) involved in the data preprocessing and microseismic noise present in the seismograms. Past ULVZ studies (e.g. Pachhai *et al.* 2014, 2015) account for correlated noise using a first-order autoregressive (AR1) noise model. In autoregressive model, the data noise or residual ($\boldsymbol{r} = \boldsymbol{d}^{\text{obs}} - \boldsymbol{d}(\boldsymbol{m})$) at current time ($r_t$) can be predicted by the residual at previous time point $t-1$ (i.e. r_{t-1}) expressed in the following form.

$$r_t = c + a r_{t-1} + \varepsilon_t, \tag{7}$$

where, c is the mean, a is the AR1 coefficient and ε_t is uncorrelated noise at time point t. The covariance matrix can be obtained from the autocovariance (A), which can be expressed in terms of AR1 coefficient (a) and standard deviation of noise (σ) (e.g. Dettmer & Dosso 2012).

$$A_l = \frac{\sigma^2}{1-a^2} a^{|l|}, \tag{8}$$

where l is the lag, and σ is the standard deviation of uncorrelated noise ($\boldsymbol{\varepsilon}$). Figs 8 and 9 show examples of autocovariance and covariance matrix, respectively, for synthetic noise.

Therefore, for the AR1 model, the noise covariance matrix can be parametrized by two parameters: correlation width (represented by AR1 coefficient, a) and standard deviation of the errors. The likelihood function for AR1 noise model is expressed in the following form.

$$L(\boldsymbol{m}) = \prod_{i=1}^{\text{nev}} \frac{1}{\left(2\pi\sigma_i^2\right)^{N_i/2}} \exp\left[-\left|\boldsymbol{d}_i^{\text{obs}} - \boldsymbol{d}_i(\boldsymbol{m}) - \boldsymbol{d}_i(a_i)\right|^2\right], \tag{9}$$

where $\boldsymbol{d}_i(a_i)$ are the AR1 predictions for AR1 coefficient represented by a_i. This is the noise parametrization we used in our past ULVZ studies. But this study considers the inversion of covariance matrix in eq. (5) as well and compares results from both parametrization of noise.

3.2 Computation of the noise covariance matrix

When analysing real data, we do not know the true noise, therefore, the data noise is approximated by the residuals, which is the difference between observed data and theoretical prediction. The parametrization of noise model using AR1 model (presented in eqs 7to 9) works well when the real data noise is explained by what we assume here as autoregressive model, but the noise characteristics are unknown and change from event to event. Therefore, noise characteristics are challenging to characterize with a few parameters. In particular, the 2.5-D synthetic seismograms (Figs 3, 4 and 7) show more information (i.e. arrivals) than those for 1-D synthetics due to full wavefield present in the 2.5-D synthetics and additional phases generated from ULVZ edges. The true theoretical noise model (i.e. autocorrelation of the difference between 2.5-D synthetic and 1-D synthetic data) can be different than the autocorrelation of noise model parametrized through AR1 coefficient. This difference is highlighted in Figs 8 and 9. Fig. 8 shows example statistical noise models prepared using the AR1 noise model with various AR1 coefficient. To prepare these noise models, we generated 1000 random realizations of noise using various AR1 coefficients (from 0.6 to 0.98) and calculated the autocorrelation of the noise which are shown in Figs 8a–f (grey lines). The average is shown (black line) compared to that for true theoretical noise model (green line). Although it may be possible to match the theoretical noise using an AR1 model, it is highly dependent on the selection of the random seed, which is not typically sampled in the inversion. Hence, the average AR1 model is insufficient to describe the noise present in the full waveform synthetics.

Fig. 9 shows the noise covariance matrix computed for the ensemble average of the AR1 models and the true theoretical noise model. There are differences in these noise models, particularly the side lobes of the autocorrelation function, which is in part due to correlated noise in the full waveform synthetics. Therefore, we propose to use a more general representation of the noise as in eq. (5). Thus, we compute the covariance matrix, $\boldsymbol{C}_{\boldsymbol{d}}$, from the theoretical residuals and use that covariance matrix in the inversion.

The noise covariance matrix can be computed from the data residuals $\boldsymbol{r} = \boldsymbol{d}^{\text{obs}} - \boldsymbol{d}(\boldsymbol{m})$. The j-th element of the autocovariance function is given by (e.g. Dettmer *et al.* 2007)

$$c_{i,j} = \frac{1}{N} \sum_{k=0}^{N-j-1} \left(r_{i,j+k} - \overline{r_i}\right)\left(r_{i,k} - \overline{r_i}\right), \tag{10}$$

where $\overline{r_i}$ is the mean of the data residuals. Every term in $c_{i,j}$ is used to build the j-th diagonal of the initial data covariance matrix $\boldsymbol{C}_{\boldsymbol{d}}$. This builds a Toeplitz or banded matrix such that every lag has a constant correlation parameter (Fig. 9). This approach has been previously applied in geoacoustics (e.g. Dettmer *et al.* 2007).

3.3 Bayesian inversion with parallel tempering

Inversion of ScP waveforms for ULVZ parameters is a non-linear problem, and there exist no analytical solutions for the PPD defined in eq. (4). Therefore, a numerical sampling algorithm such as Markov Chain Monte Carlo (MCMC) is considered to estimate the PPD numerically. Sampling algorithms such as MCMC can be inefficient for highly non-linear problems, particularly when two or more high probability regions are separated by a low probability region. In that case, MCMC may explore local minima without converging to the global minima. To improve the sampling efficiency and converge to the global minima, we apply interacting MCMC, also known as parallel tempering. In parallel tempering, a ULVZ model is randomly proposed from a uniform prior in each iteration. Then the proposed model is accepted or rejected with probability (α). If $q(\boldsymbol{m}', \boldsymbol{m})$ is the distribution for a proposed transition from the current model ($\boldsymbol{m}$) to a new model ($\boldsymbol{m}$), the proposed model is then accepted or rejected using the following probability.

$$\alpha = \min\left[1, \frac{p(\boldsymbol{m}')}{p(\boldsymbol{m})}\left(\frac{L(\boldsymbol{m}')}{L(\boldsymbol{m})}\right)^{\beta} \frac{q(\boldsymbol{m}, \boldsymbol{m}')}{q(\boldsymbol{m}', \boldsymbol{m})}\right], \tag{11}$$

where β is the tempering parameter used for parallel tempering and is the reciprocal of the temperature width (dT). In eq. (5), the priors do not change, i.e. $p(\boldsymbol{m}') = p(\boldsymbol{m})$, and proposals ($q(\boldsymbol{m}, \boldsymbol{m}')$, and $q(\boldsymbol{m}', \boldsymbol{m})$) are symmetric, therefore, the acceptance/rejection probability becomes $\left(\frac{L(\boldsymbol{m}')}{L(\boldsymbol{m})}\right)^{\beta}$.

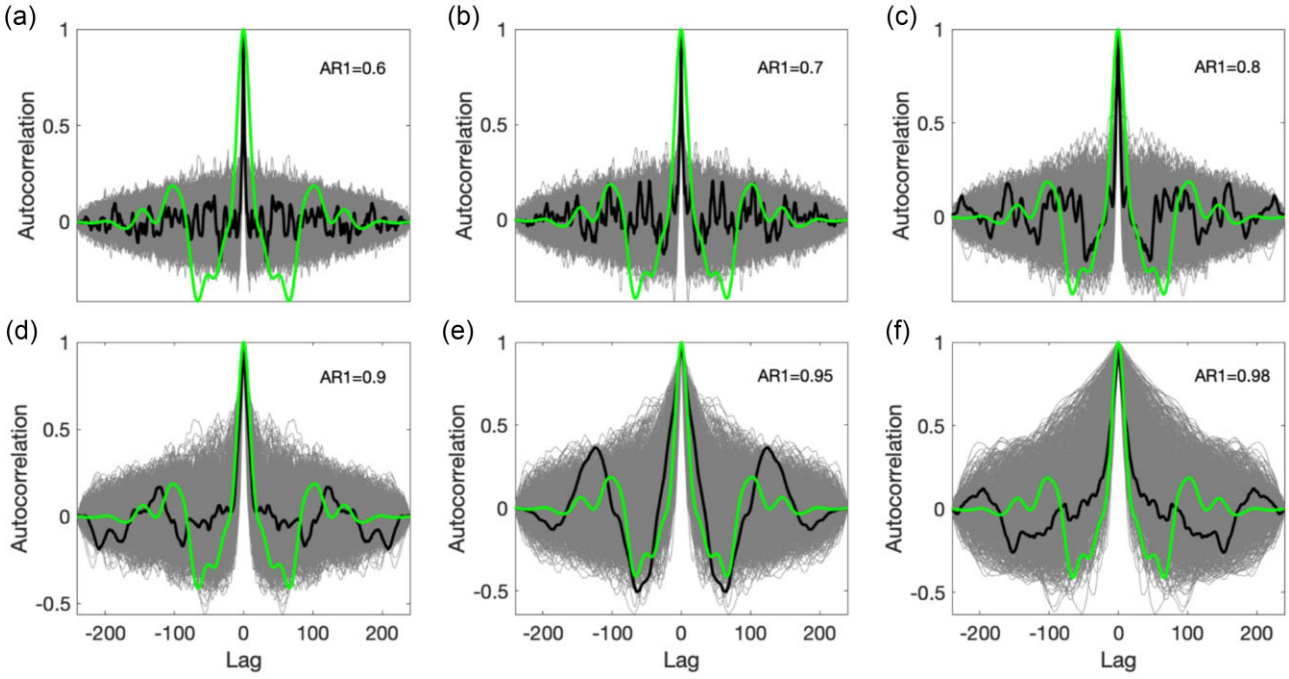

Figure 8. Autocorrelation function for AR1 coefficients of (a) 0.6, (b) 0.7, (c) 0.8, (d) 0.9, (e) 0.95 and (f) 0.98 compared with the ensemble average of 1000 noise models (black line), and the theoretical noise (green line). We define true theoretical noise as the difference between the ScP waveforms obtained using 1-D forward and 2.5-D forward computation.

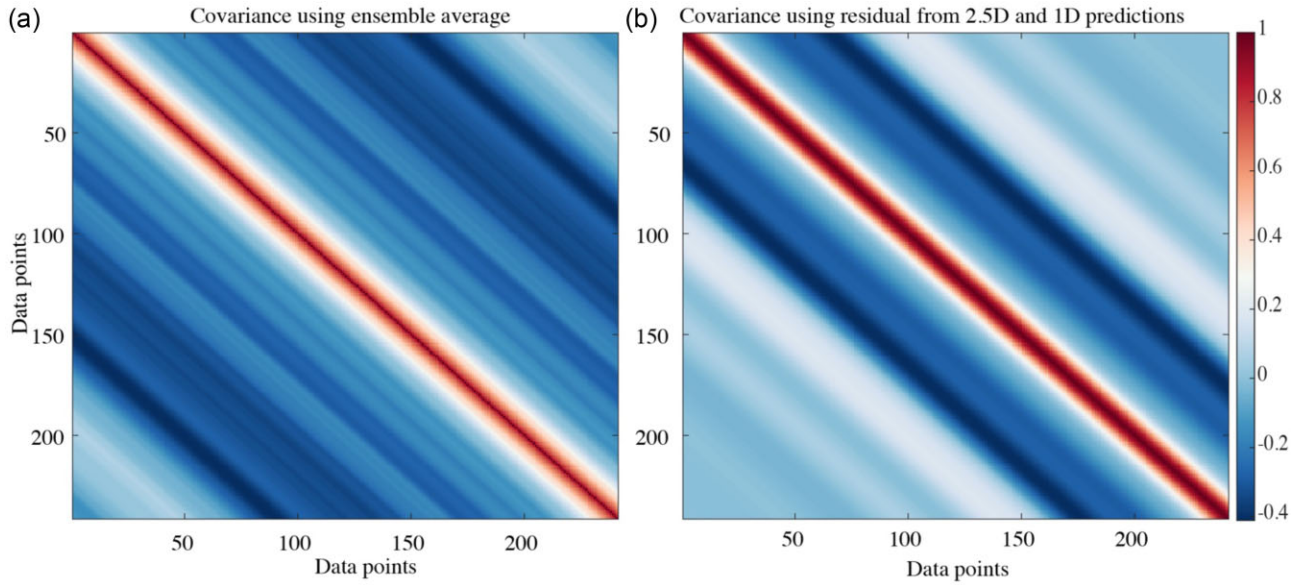

Figure 9. Covariance matrix computed from (a) the ensemble average of the noise computed for AR1 = 0.98, and (b) from the theoretical errors presented in Fig. 8. Colourbar represents the normalized covariance.

In parallel tempering, MCMC are performed on a series of chains with different β-values. The chains with lower values of β decrease the likelihood function in eq. (5) resulting in wider exploration of the parameter space while chains with high β-values preferentially sample high posterior probability regions. To get the unbiased samples from the PPD, parameter inferences are made based on a chain with $\beta = 1$. Parameters from randomly selected chain pairs are proposed to swap/exchange between chain pairs after performing MCMC sampling within-chain. For example, suppose $\boldsymbol{m}_t^i$ are the parameters of the chain i and $\boldsymbol{m}_t^j$ are the parameters of the chain j at t-th iteration. Then parameter swap between two chains i and j is proposed which is accepted or rejected based on the Metropolis Hasting acceptance probability (α_β; Gilks & Roberts 1996) defined by;

$$\alpha_\beta = \min\left(1, \frac{p_i\left(\boldsymbol{m}_t^j\right) p_j\left(\boldsymbol{m}_t^i\right)}{p_i\left(\boldsymbol{m}_t^i\right) p_j\left(\boldsymbol{m}_t^j\right)}\right), \tag{12}$$

where $p_i(\boldsymbol{m})$ is tempered target distribution given by, $p_i(\boldsymbol{m}) = [p(\boldsymbol{m})]^{\beta_i}$.

Parameter values are exchanged and updated to proceed for the next iteration if the proposed swap is accepted. In contrast, the parameter values are retained in both chains if the proposed swap is rejected. Then the sampling is proceeded for the next iteration. This procedure allows the algorithm to take advantage of the various ranges of exploration scales without biasing the PPD.

In this paper, we start inversion with an arbitrary model in each of 12 cores with the logarithmic spacing of the tempering levels set to 1.35. All parallel tempering chains are repeatedly refocused on the best model and final samples are collected from one chain, which is not tempered and provides unbiased sampling. For each randomly drawn model, synthetic ScP waveforms are computed using the WKBJ method (Chapman & Orcutt 1985) and convolved with the STF, and the likelihood values are computed in a 20-s window around the central peak of ScP (5 s before and 15 after). The likelihood for the current model is compared to the likelihood for the previous model scaled by the tempering parameter. Then a random number between 0 and 1 is drawn. If that random number is smaller (greater) than the likelihood ratio, the model is accepted (rejected). We update the model and continue for the next iteration if the proposed model is accepted. In contrast, we retain the model and propose again if the model is rejected. This process is iterated many 100′s of thousands of times and the first 1/3 of the samples are discarded as burn-in period to remove the dependence of MCMC on the starting point. For more details, we refer to previous studies (Pachhai *et al.* 2014, 2015, 2023). Samples after the burn-in period are considered for parameter inference. We monitor the convergence of the algorithm by examining the sampling history for various parameters by comparing inferences for the first third of PPD samples (from post burn-in) to inferences for the last third. When no significant differences exist in the marginals of parameters, the sampling is considered to have converged.

4 FEASIBILITY OF BAYESIAN INVERSION USING NOISE COVARIANCE MATRIX

To test the feasibility of using the covariance matrix representation of noise we conducted several synthetic experiments. In the first experiment, we computed a synthetic ScP waveform for a 20-km thick 1-D ULVZ with a 10 per cent decrease in V_P, a 30 per cent decrease in V_S and a 10 per cent increase in density with respect to the ak135 (Kennett *et al.* 1995) 1-D model using the WKBJ method. Then the correlated noise with AR1 parameter 0.95 and noise standard deviation 0.05 was added to the synthetic ScP data. The synthetic seismograms with and without noise and their autocorrelations are shown in Fig. 10(a), which shows a strong correlation of residuals. We calculated the covariance matrix using eq. (10). The covariance matrix is shown in Fig. 10(b), and this covariance matrix is used to compute the likelihood in eq. (5). Fig. 10(c) shows the inversion results in terms of profile marginal densities for different ULVZ parameters. Profile marginal densities are obtained by considering only the parameter of interest as a function of height above the CMB while integrating out all other parameters in the PPD. In this process, the height above the CMB is discretized and we choose to normalize each depth interval individually. Fig. 10(c) indicates that the true model parameters (indicated by black and white dashed lines) are well recovered with wider uncertainties for density due to its weaker sensitivity to the ScP in comparison to other parameters.

For our second feasibility test, we considered synthetic ScP waveforms computed for a 2.5-D boxcar shaped ULVZ of length $l = 6^\circ$ and edge positioned at $l_1 = 2^\circ$ and $l_1 = 8^\circ$. When $l_1 = 2^\circ$, the ScP ray does not directly hit the ULVZ while in the case of $l_1 = 8^\circ$ the ScP ray hits the ULVZ near the centre of the boxcar from the top (Fig. 2b). The waveforms are shown in Fig. 3. We test both cases using the AR1 model and the covariance matrix method of noise parametrization.

Inversion results using covariance matrix and AR1 parametrization of noise are shown in Fig. 11 for 2° and 8° edge locations. Inversion results using both approaches, for a ULVZ with $l_1 = 2^\circ$, show that the ULVZ parameters are highly uncertain as the ScP ray does not hit the ULVZ (Figs 11a and b). Regardless of which noise model is used, the *S*-wave velocity recovered is near 0 per cent and the ULVZ height is spread out over the range of priors. When $l_1 = 8^\circ$, the inversion recovers the ULVZ height, δV_S, and δV_P when using the noise covariance matrix. In this case the density perturbation is highly uncertain (Fig. 11d). In contrast, the inversion using the AR1 model recovers incorrect ULVZ model parameters with a thin (∼5 km) and $\delta V_P \approx$ -10 per cent and $\delta V_S \approx$ -40 per cent. The AR1 model gives much narrower uncertainties than when we use the noise covariance matrix in the inversion.

We further explore the feasibility of our inversion approach using synthetics for a boxcar shaped ULVZ model. The ULVZ model has elastic parameters of $\delta V_S =$ -20 per cent, $\delta V_P =$ -10 per cent and $\delta\rho = +5$ per cent. This ULVZ has a height of 20 km with a constant length of $l = 8^\circ$ and l_1 edge positions from 2° to 14° in 0.5° increments. For this model the ScP ray path directly strikes the ULVZ for edge positions l_1 from ∼3.5° to 11.5°. We followed the same procedure described earlier to invert these synthetics using two inversion approaches (AR1 and covariance matrix) presented in Section 3. The inversion results are presented in Figs 12(a)–(d). Results from both inversion methods show narrower uncertainties for h and δVs in comparison to that for $\delta\rho$ and δVp. This is due to the weaker sensitivity of ScP to those parameters. As discussed in Pachhai *et al.* (2023), the ScP waveforms are most sensitive to δV_S and h, and thus we focus our discussion in the rest of this paper on those parameters and present the results for $\delta\rho$ and δVp in the supplementary material (Figs S1–S6). Supplementary material also shows the comparison of inversion results using AR1 approach and covariance matrix approach for all the 2-D models presented in Table 1 (Figs S1–S6). Although the uncertainties are smaller for all ULVZ parameters when we consider AR1 noise model in the inversion, the true values for those parameters are not within the uncertainties of the recovered models in most cases. ULVZ parameters are not recovered even when the ScP ray directly strikes the top of the ULVZ (Fig. 12). For the covariance matrix method, the uncertainties are larger and typically encompass the true elastic parameters when the ScP ray directly strikes the ULVZ. When the ScP ray is near the ULVZ boundaries (∼3.0° and 11.0°) the covariance matrix method also cannot recover the true parameter values. This is because of the multipathed ScP arrivals observed for these positions. In this example there is an additional edge location (∼6.5°), where the inversion does not recover the ULVZ parameters due to the constructive interference of Sl_2P with the ScsP phase. Overall, the covariance matrix method outperforms the AR1 based method. In what follows, we focus our discussion on just the covariance-based method, and similarly to Pachhai *et al.* (2023), we perform the inversion using multiple seismic traces in a joint inversion to best determine how well this method can be used to recover ULVZ parameters

In the synthetic experiments presented above (Figs 10–12), we carried out the inversions assuming a known noise covariance matrix. However, we do not know the true noise covariance matrix

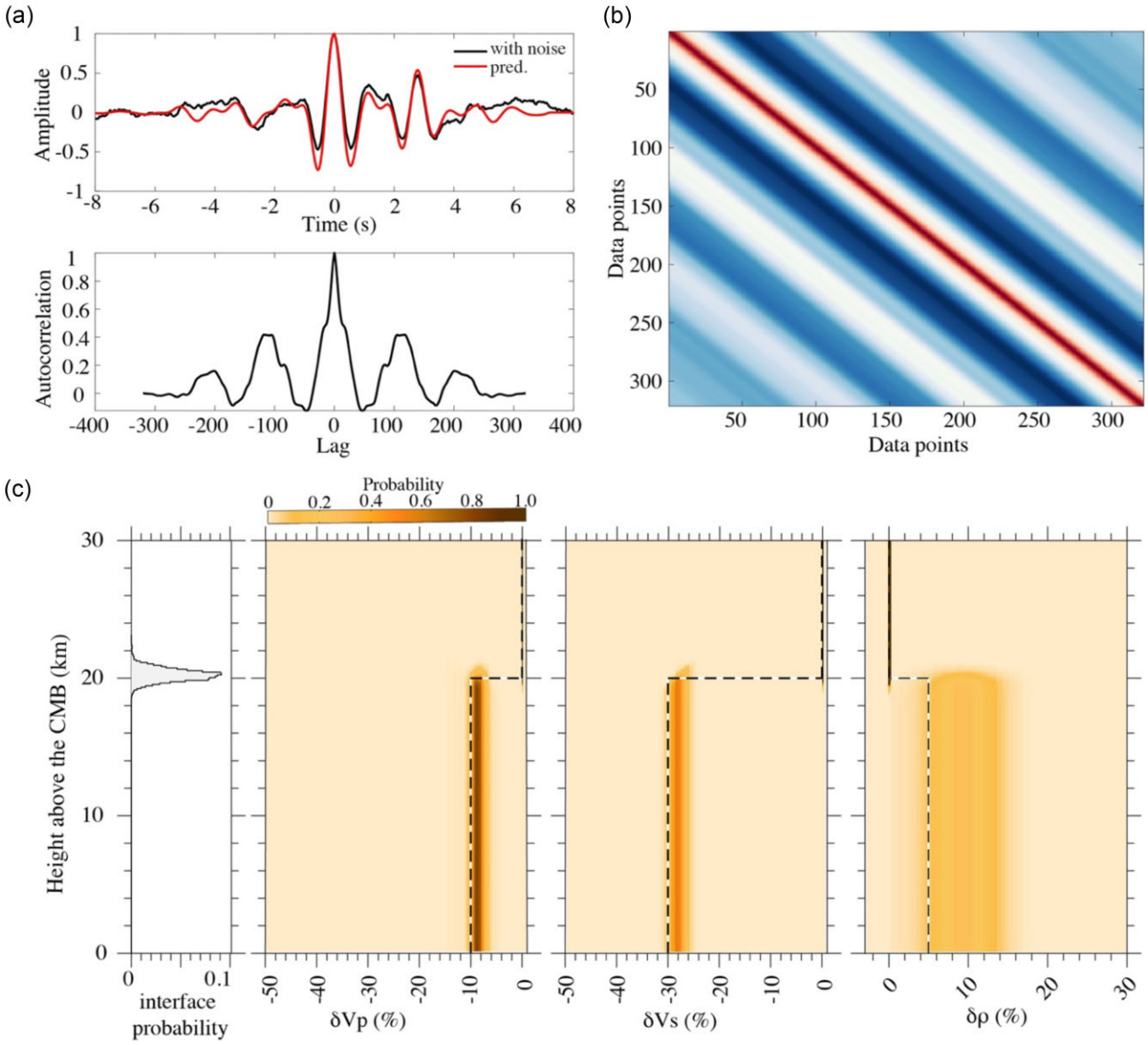

Figure 10. (a) Synthetic data with (black line) and without (red line) noise and autocorrelation of correlated noise prepared for AR1 = 0.95 and standard deviation ($\sigma = 0.01$). (b) Noise covariance matrix computed using eq. (6) for the AR1 noise. (c) Inversion results expressed in terms of posterior probability of interface, δV_P, δV_S, and $\delta\rho$ as a function of height of ULVZ above the CMB. The black and white dashed lines indicate the true model.

when inverting real data. Therefore, our final feasibility experiment is performed with an unknown covariance matrix. For this experiment, we first computed a predicted ScP waveform for the same ULVZ model considered in the first experiment, but we did not add any noise to the synthetics. Then the noise covariance matrix in eq. (10) was computed using residuals between the true model prediction and the predictions for the ak135 model. In other words, we start out by forcing the ULVZ-related waveform features to be considered as noise in the covariance matrix. Then we run the inversion using this wrong covariance matrix in the inversion.

The inversion results, in Fig. 13(a), show that the recovered models are broadly distributed within the prior range for δVp and $\delta\rho$. The true ULVZ parameters are within uncertainties for δV_S and h that are narrower than that for the other two parameters but still widely uncertain. We next extracted the maximum-likelihood model from the first inversion and updated the covariance matrix using the residuals between the observation (i.e. true ULVZ model prediction in this case) and the maximum-likelihood model predictions. The inversion results for this second inversion are shown in Fig. 13(b). In the second inversion all of the ULVZ parameters are recovered with reasonable uncertainties (Fig. 13b), but we note that the uncertainties are smaller than those of the first experiment (Fig. 10c) because there is no additional noise in this experiment. This experiment illustrates this method can recover the true model using an iterative approach to updating the noise covariance matrix, even when the starting noise covariance matrix is far from the true noise covariance matrix.

5 2.5-D SHAPE EFFECTS ON THE INVERSION OF ULVZ PARAMETERS

To further assess how 2.5-D ULVZ shapes affect the estimation of ULVZ parameters using 1-D modelling, we computed ScP synthetic seismograms for a series of 2.5-D ULVZ models of various

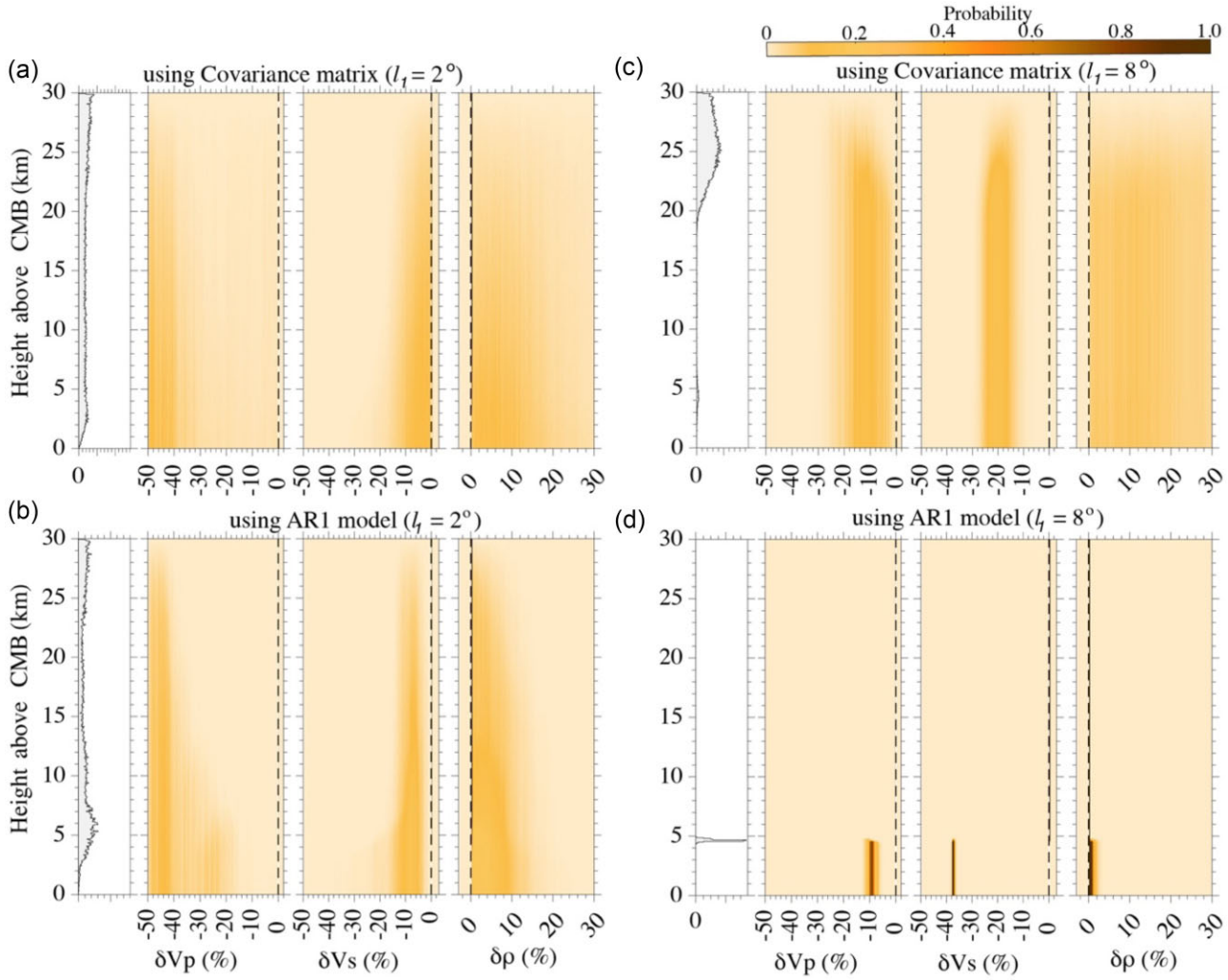

Figure 11. Inversion results for a boxcar ULVZ of 6° length with left edge located at 2° (a) using noise covariance matrix and (b) using AR1 noise model in the inversion. Other ULVZ parameters are: $h = 25$ km, δVs = -20 per cent, δVp = -10 per cent and $\delta\rho = 5$ per cent. (c) and (d) Same as (a) and (b) but for a ULVZ with left edge located at 8°.

lengths and edge locations presented in Table 1. Because of the high computational cost of computing high frequency ScP waveforms, we concentrate this study on just a handful of models, focusing on changing the ULVZ length in the great circle arc direction ($l = 4°$, 6°, 8° or 12°) and on how shapes (boxcar, Tukey or Gauss) affect the solutions. The elastic parameter of these ULVZs are δV_S = -20 per cent, δV_P = -10 per cent and $\delta\rho = +5$ per cent and are the same as those inferred, using a 1-D approach, beneath the Coral Sea (Pachhai *et al.* 2023). We use these elastic parameters as a basic test case so that we can compare results from this study to the previous data analysis.

In the previous section we analysed the effect of 2.5-D ULVZ morphologies on the inversion results using single ScP waveform from one edge location (see Figs 11–12) and applied both inversion approaches for all the ULVZ models presented in Table 1. However, Pachhai *et al.* (2023) found more robust estimation of ULVZ parameters when multiple waveforms are simultaneously considered in the inversion. Here we consider waveforms from three edge locations simultaneously with edge locations within 1° of each other treating them as if the multiple events strike the ULVZ at different edge locations. For example, three ScP synthetic waveforms with edge locations $l_1 = 2.0°$, 2.5° and 3.0° are used to perform the inversion for representative edge location $l_1 = 2.5°$. Similarly, three waveforms from $l_1 = 2.5°$, 3.0° and 3.5° are considered for the inversion of $l_1 = 3.0°$. The simultaneous inversion of three waveforms from 1° separation of edge locations was determined by the size of the ScP Fresnel zone of 1° across and is the size of the geographic bins used in Pachhai *et al.* (2023).

5.1 Effect of Boxcar shape

To examine how well the inversion techniques can recover ULVZ parameters when the wavefield is computed for 2.5-D finite length ULVZ models, we perform the inversion with two different setups for the noise covariance matrix. In the first setup we assume the true 1-D ULVZ model prediction to use in computing the noise covariance matrix. In the second setup, we make no assumptions and perform the inversion iteratively, starting with ak135 predictions. The first setup tests our ability to recover ULVZ parameters in the best-case scenario. And thus, challenges encountered here are inherent to challenges associated with the 2.5-D wavefield. The second

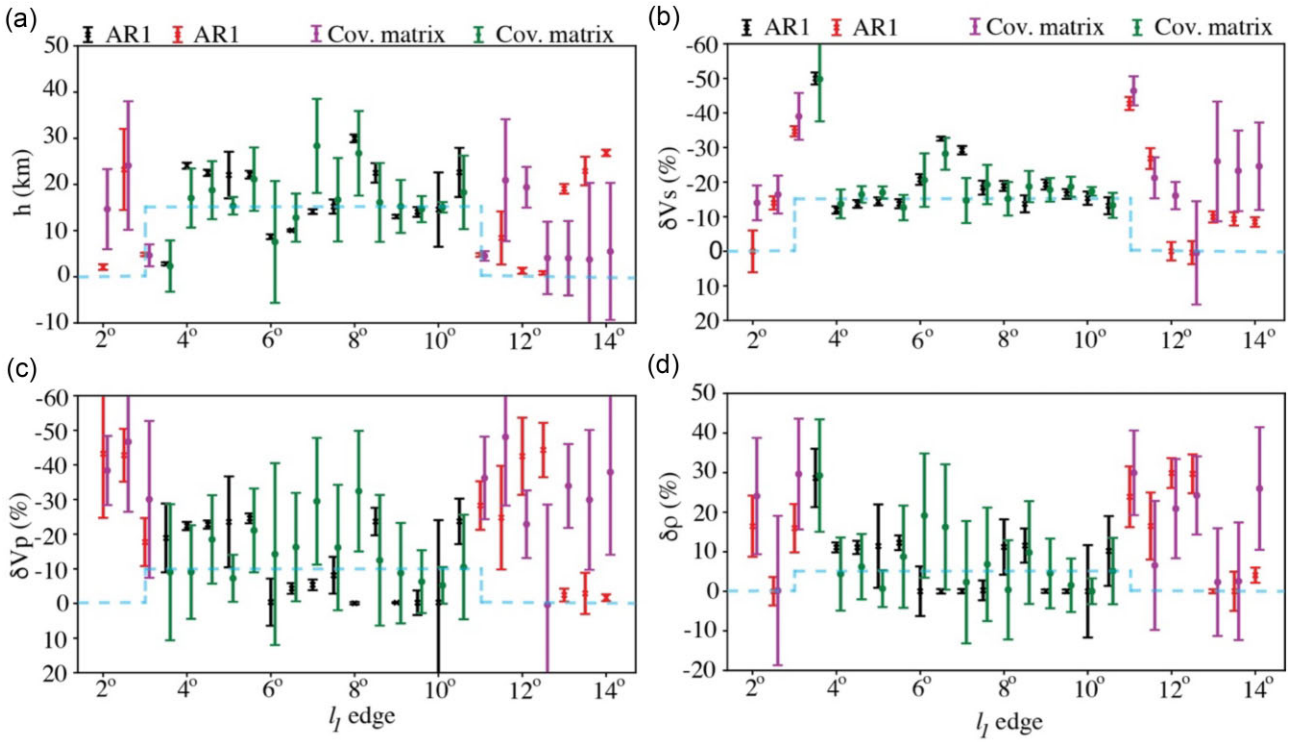

Figure 12. The inversion results for (a) thickness, (b) *S*-wave velocity perturbation (δVs), (c) *P*-wave velocity perturbation (δVp) and (d) density perturbation ($\delta\rho$) with 2 standard deviations retrieved for the boxcar (B4, see Table 1) model using AR1 noise model (black) and covariance noise model (green) in the inversion. Results using noise covariance matrix are slightly shifted right for visualization purpose only. Horizontal light-blue colour dashed lines represent the true values of ULVZ parameters and vertical dashed lines indicate the l_1 edge boundaries within which ScP hits the ULVZ. The black and green error bars represent the ULVZ parameters recovered within a region of boxcar where ScP strikes the ULVZ while the magenta and red colour error bars represent the ULVZ parameters recovered from the regions where ScP does not strike the ULVZ including edges.

Table 1. Various 2-D ULVZ models computed for 1-D inversion test.

Model	δV_S (per cent)	δV_P (per cent)	h_{max} (km)	$\delta\rho$ (per cent)	l	l_1 edge	Shape
B1	−20	−10	25	+5	6°	2°–14°	Boxcar
B2	−20	−10	15	+5	6°	2°–14°	Boxcar
B3	−20	−10	15	+5	4°	2°–14°	Boxcar
B4	−20	−10	15	+5	8°	2°–14°	Boxcar
T1	−20	−10	15	+5	4°	2°–14°	Tukey
T2	−20	−10	15	+5	6°	2°–14°	Tukey
T3	−20	−10	15	+5	8°	2°–14°	Tukey
T4	−20	−10	15	+5	12°	2°–14°	Tukey
G1	−20	−10	15	+5	6°	2°–14°	Gaussian
G2	−20	−10	15	+5	12°	2°–14°	Gaussian

setup tests our ability to recover ULVZ parameters in the worst-case scenario, and also more similar to what is encountered when inverting real data, where we know nothing about the structures and the noise covariance matrix a priori.

5.1.1 Boxcar shaped ULVZ with known noise covariance matrix

To study the effect of various boxcar shapes, we first computed the synthetic waveforms for a 1-D ULVZ with the same elastic properties and height for the ULVZ edge locations where ScP directly strikes the ULVZ. For ULVZ edge locations where ScP does not hit, we computed synthetics using the ak135 model. Then the difference between the 1-D and 2.5-D synthetics was computed followed by the computation of the covariance matrix using eq. (10). The 2.5-D synthetic data were considered as data, and 1-D ULVZ elastic parameters and height were sampled in the inversion. We then ran inversions of three 2.5-D synthetic waveforms (from three edge locations) simultaneously using the covariance matrices computed for those three waveforms. As described earlier in Section 5, the waveforms from three edge locations represent the central edge location. For example, three ScP synthetic waveforms with edge locations $l_1 = 2.0°$, $2.5°$ and $3.0°$ are used to perform the inversion for representative edge location $l_1 = 2.5°$. Similarly, three waveforms from $l_1 = 2.5°$, $3.0°$ and $3.5°$ are considered for the inversion of $l_1 = 3.0°$. Fig. 14 shows the inversion results for h and δV_S for the four boxcar models considered in this study (see Table 1). Results for δVp and $\delta\rho$ are shown in the supplementary material (Fig. S7).

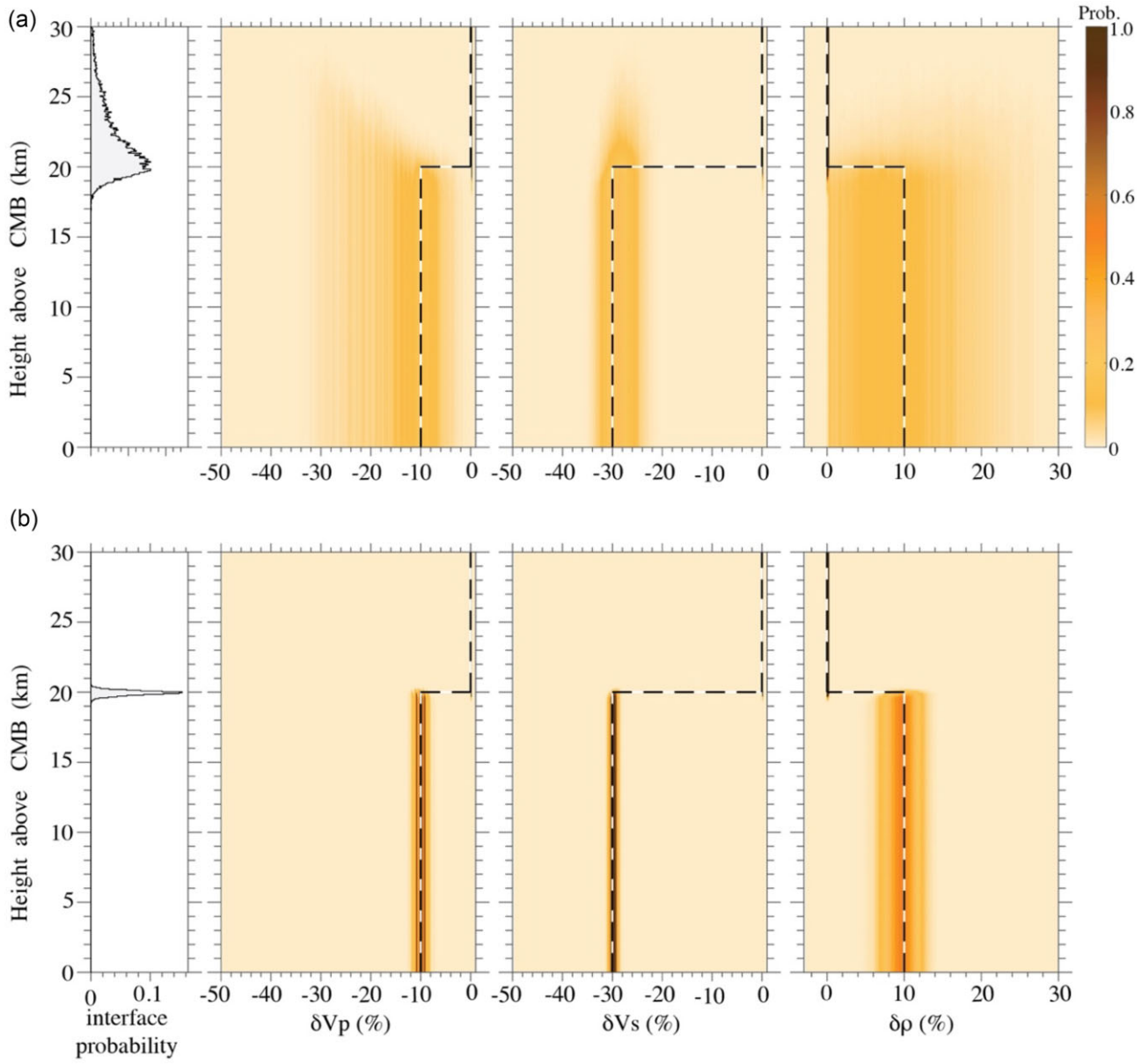

Figure 13. (a) Same as Fig. 10(c) but using wrong covariance matrix (computed from the difference between the predictions of true ULVZ and non-ULVZ models) in the inversion. (b) Same as (a) but using the covariance matrix computed from the difference between predictions of the true ULVZ model and the MAP model extracted from the first inversion in (a). True models are indicated by black and white dashed lines.

In Fig. 14 the edge locations where ScP directly hits the ULVZ from the top is represented by the blue dashed line boxcar. The recovered ULVZ parameters with uncertainties are plotted in black (red) colour for ULVZ parameters within (outside including edges) the ScP hitting area. For example, in Fig. 14(a), the ScP bounce point strikes the ULVZ between ∼5.0° and ∼11.0° (for ULVZ of $l = 6°$), whereas in Fig. 14(e), the ScP bounce point strikes the ULVZ between ∼7.0° and ∼11.0° (ULVZ of $l = 4°$). In general, we see that when the ScP bounce point strikes the ULVZ we recover the correct ULVZ parameters with small error bounds. Exceptions occur when the Sl_1P arrival constructively interferes with the ScsP post-cursor (e.g. Fig. 14a $l_1 = 8.5°$, and Fig. 14g $l_1 = 7.5°$). In this same distance range, we also recover the correct *S*-wave velocity for most models. The *S*-wave velocity is recovered better for larger model lengths (e.g. Fig. 14h, with $l = 8°$ as opposed to Fig. 14f with $l = 4°$). In all these positions, SPcP precursors are observed in the synthetics.

When the ScP bounce point is on the opposite side of the ULVZ (the smallest edge positions, e.g. $l_1 = 2°$, 3°, etc.) and does not strike the ULVZ, the wavefield still interacts with the ULVZ and we observe a weak ScsP post-cursor for most distances. There also appears to be a low amplitude negative polarity post-cursor just after ScP (Fig. 3). As a result, our inversions suggest a non-zero ULVZ thickness and δV_S in many cases. For both h and δV_S the uncertainties are much larger than in the areas where ScP directly hits the ULVZ with some exception. For example, 2.5° edge location in the case of B1 and B2 and 2.5°–5.5° edge locations in the case of B3 models have narrower uncertainties for thickness due to the similarities between the three waveforms from three nearest edge locations which are simultaneously considered in the inversion

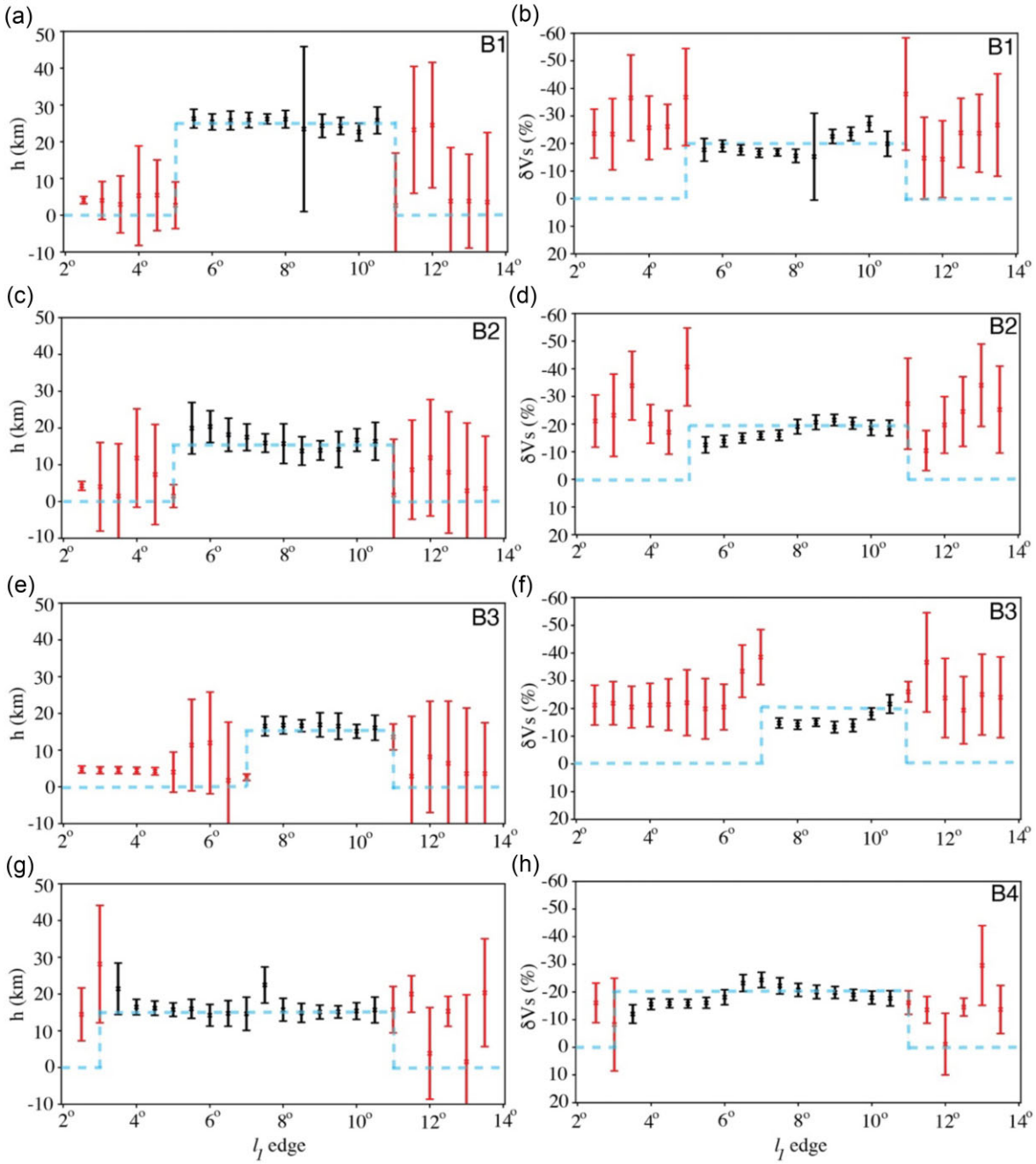

Figure 14. (a, c, e, g) Thickness (h) and (b, d, f, h) *S*-wave velocity perturbation (δVs) with their uncertainty (2-standard deviation) retrieved from the inversion of 2.5-D synthetic seismograms prepared for four boxcar models of various width and edge locations presented in Table 1 using full noise covariance matrix in the inversion. The edge locations along the x-axis in all subplots represent the average over three consecutive edge locations. The horizontal light blue dashed lines represent the true values of ULVZ parameters and vertical dashed lines indicate the l_1 edge boundaries within which ScP strikes the ULVZ. The black error bars represent the ULVZ parameters recovered within a line where ScP hits the ULVZ while the red color error bars represent the ULVZ parameters recovered from the line where ScP does not directly hit the ULVZ including edges.

and due to similarity between the 2.5-D synthetics and non-ULVZ model prediction. When the ScP bounce point is on the near side of the ULVZ (largest edge positions with $l_1 \geq 11.5^\circ$) the upgoing *P* wave from ScP interacts with the ULVZ generating more post-cursor arrivals. Similar to the previous case, we recover non-zero h and δV_S with larger uncertainty for most edge positions. We note that in these cases we do not observe SpcP pre-cursors in the synthetics.

5.1.2 Boxcar shaped ULVZ with unknown noise covariance matrix

We further inverted for all boxcar ULVZ models using the iterative approach with the ak135 model predictions used to initialize the noise covariance matrix. We did two iterations, where the second iteration was run using the covariance obtained for the residuals between the observations (2.5-D ULVZs in this case) and maximum-likelihood model predictions from the first inversion. The inversion results for the first iteration are not shown here, but the results for

the second iteration are shown in Fig. 15 for h and δVs and in Fig. S8 for $\delta\rho$ and δVp. The inversion results outside of the boxcar do not change significantly, but results (both maximum-likelihood model and uncertainties) inside the boxcar are different than those using the true noise covariance matrix. This is because the 1-D ULVZ like signals resulting from the 2.5-D ULVZs were mapped as noise in the covariance matrix in the case when we consider true noise covariance matrix.

When we use the iterative approach, the inversion occasionally recovers the thickness and S-wave velocity decrease (δVs) (Figs 15a and b) but is strongly affected by the additional multipathing and edge arrivals. The ULVZ parameters are best recovered for the thinner, larger length ($h = 15$ km, $l = 12^\circ$, Figs 15g–h) models. As the length decreases the effects of the extra multipath arrivals and interference with edge arrivals becomes more prominent, with a general tendency to underpredict the ULVZ thickness with a general increase in S-wave velocity. The sharp boxcar morphology generates the strongest multipath arrivals and most impulsive edge arrivals. But it is unlikely that ULVZs exhibit the sharp boxcar morphology in the real Earth, so this case may represent the end member scenario of what we can recover in the worst case.

5.2 Effect of Tukey shape

5.2.1 Tukey window shaped ULVZ with known noise covariance matrix

We also computed synthetic seismograms for ULVZ models with Tukey shapes (Table 1). We inverted these models for ULVZ parameters as described in Section 5.1. Fig. 16 shows the inversion results for h and δVs and Fig. S9 shows the inversion results for $\delta\rho$ and δVp when we used the known covariance matrix in the inversion. For the shortest length model (model T1 with $l = 4^\circ$, Figs 16a and b), the δVs is poorly retrieved (Fig. 16a) even at the edge locations where ScP strikes the middle of the ULVZ. This is due to the existence of multipath ScP arrivals, Sl_1P and Sl_2P, all of which are interfering with ScsP in this case. But as we increase the length of the Tukey model (going from $l = 4^\circ$ in Fig. 16a to $l = 12^\circ$ in Fig. 16g), the ULVZ parameters are better recovered. Similar to the boxcar shaped models, smaller uncertainties in parameters are recovered when the ScP ray hits the flat part of the ULVZ from the top. But when the ScP ray misses the ULVZ or is in the transition zone up to the flat part, we still retrieve ULVZ structure, albeit with larger uncertainties, in the inversion due to the persistent existence of ULVZ post-cursor energy in the wavefield. Again, SPcP precursors are also observed when the ScP ray path directly hits the flat part of the ULVZ from above. The true values of the models are well recovered for the longest models (approaching a reasonable 1-D approach), except at the boundaries where the ULVZ edges have a large slope. These locations are dominated by large uncertainties.

5.2.2 Tukey window shaped ULVZ with unknown noise covariance matrix

The inversion results for the Tukey shaped window are shown in Fig. 17 for h and δVs and Fig. S10 for $\delta\rho$ and δVp. For the Tukey shaped models, the iterative inversion approach recovers thinner ULVZ and stronger δVs for almost all cases where the ScP bouncepoint is within the ULVZ (Figs 17a–d). Here the post-cursor is amplified because of constructive interference between the post-cursor and conversions from l_1 and l_2 edges (i.e. Sl_1P, Sl_2P, see Fig. 7a for the waveforms). The shape of the Tukey window generates longer period edge arrivals than the impulsive arrivals generated by the boxcar model. As the inversion fits a larger amplitude post-cursor, the ULVZ height must become thinner in the 1-D inversion. This effect is reduced when the length of Tukey ULVZ becomes larger (Figs 17e–h) because the ScsP post-cursor and post-cursors related to edge locations (Sl_1P and Sl_2P) start to separate.

5.3. Effect of Gaussian shape

5.3.1 Gaussian shaped ULVZ with known noise covariance matrix

We also tested the inversion against the Gaussian shaped ULVZ models, and the inversion results are shown in Fig. 18 for h and δVs and in Fig. S11 for $\delta\rho$ and δVp. For the 6° length model the ULVZ thickness matches the maximum height of the Gaussian shape from $l_1 = 7^\circ$ to 10° which is a reasonable approximation of the overall ULVZ width. One might interpret this as a flat topped ULVZ however, with little indication of the Gaussian shape. Outside of this edge range, the uncertainty in thickness increases significantly as there is no post-cursor like signal. The S-wave velocity is well recovered for all edge positions, with a small increase in uncertainty for edge positions that miss the ULVZ. For a Gaussian ULVZ with a 12° length, the ULVZ parameters recovered for edge locations from $l_1 = 3^\circ$ to 11° are particularly good. This case looks more similar to the boxcar and Tukey window shaped ULVZs presented previously, where the uncertainty becomes quite large when the ScP bouncepoint is outside of the ULVZ. As in those cases, we observe an SPcP precursor for the Gaussian shaped ULVZ models when the ScP ray directly strikes the ULVZ.

5.3.2 Gaussian shaped ULVZ with unknown noise covariance matrix

We also performed inversion of all the 2.5-D Gaussian synthetics using the iterative approach. The inversion results are shown in Fig. 19 for h and δVs. The inversion results for $\delta\rho$ and δVp are shown in Fig. S12. In contrast to the boxcar and Tukey window, δVs is well recovered for both Gaussian models (Figs 19b–d). The thickness and the 2-D shape of the Gaussian ULVZ is closely recovered for 12° length (Fig. 19c). However, the thickness of the shorter Gaussian ULVZ is poorly recovered (Fig. 19a), particularly for shorter edge locations below 8°. This is because there are no visible post-cursors like signals before the 8° edge locations. The Gaussian shaped ULVZs still generate Sl_1P and Sl_2P arrivals, but these are lower amplitude than in the boxcar or Tukey shaped ULVZs and do not provide as strong a constructive interference in the post-cursor wavefield.

6 RESULTS FOR OBSERVED DATA

From our synthetic experiments, we found that the inversion of ULVZ parameters works better if we incorporate the noise covariance matrix in the inversion in comparison to that parametrized using the AR1 model and when we include multiple events in the inversion. We then applied both approaches to observed data from three geographic bins sampling the CMB beneath the Coral Sea that were previously analysed in Pachhai *et al.* (2023). Bin locations considered in this study are indicated by stars with different colours in Fig. 1(a). Individual ScP waveforms for each event were bandpass filtered with corners at 0.5 and 1.5 Hz. Then the P and

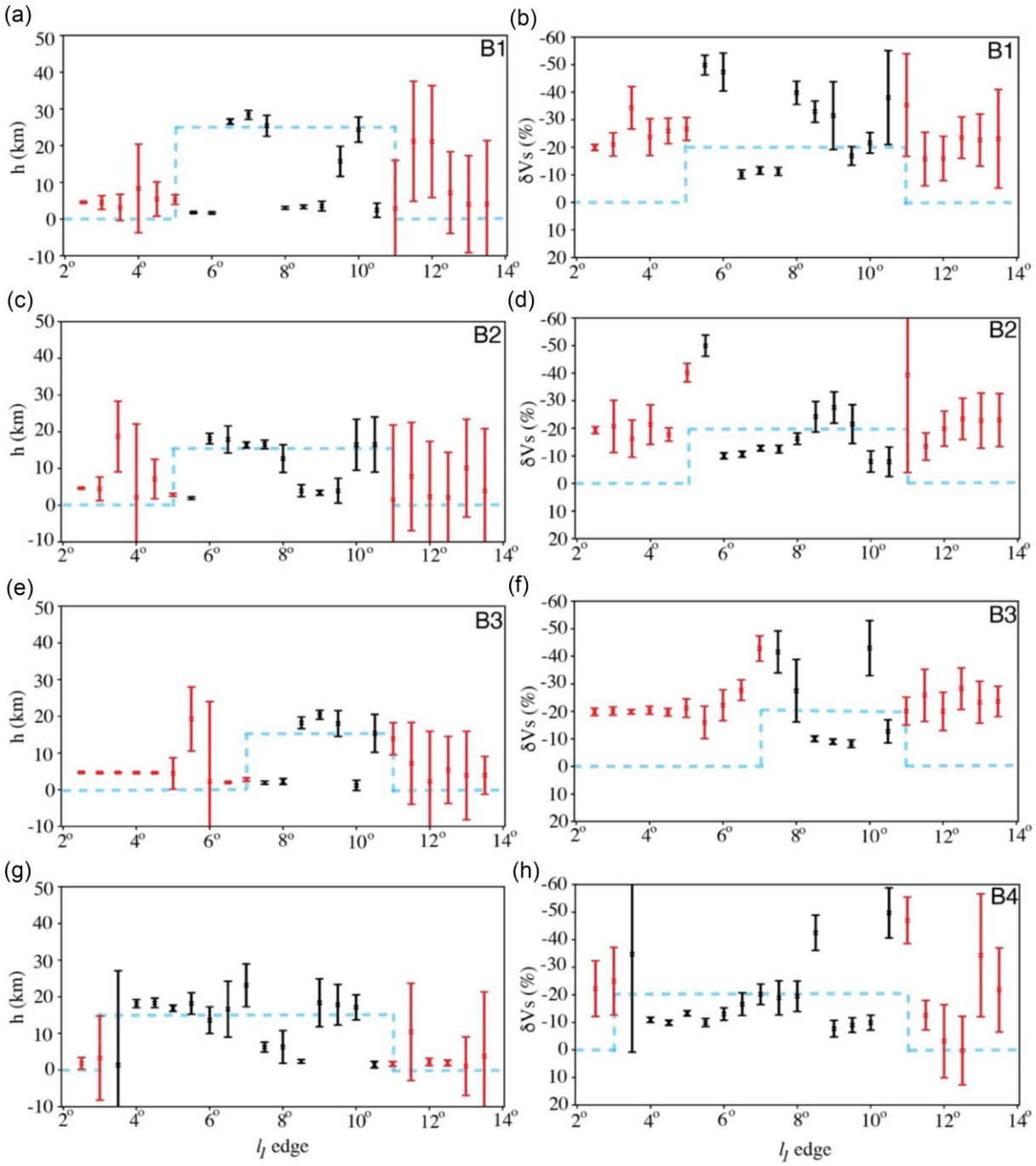

Figure 15. Same as Fig. 14, but the inversion was run using the covariance matrix computed for the residuals between 2.5-D ULVZ predictions and predictions for the maximum-likelihood model obtained from the first inversion. The first inversion was run using the covariance matrix computed for the residuals between 2.5-D ULVZ predictions and predictions for AK135 model.

ScP waveforms were aligned and stacked using the adaptive stacking approach (Rawlinson & Kennett 2004), separately. Then the events were grouped into bins based on their sampling at the CMB. We refer to Pachhai *et al.* (2023) for more details on the data processing.

We selected these specific bins as they have been previously presented and analysed in Pachhai *et al.* (2023), and we wanted to compare the results from the previous study that parametrizes noise covariance matrix using the AR1 model to the results from this study, which includes full data noise covariance matrix in the inversion. The ScP wavelets and *P* wavelets (considered as STF) for three bins are shown in Fig. 20. Bins 37, 24 and 41 have waveforms from 14, 13 and 27 events, respectively. In all of these bins, ScP waveforms are more complex than the *P* wavelet, however, the level of complexity is dependent on the event. Bin 41 shows simple waveforms that appear well explained by the direct *P* wavelet. Whereas Bins 24 and 37 appear to show low amplitude ScP pre- and post-cursor arrivals. Bins 37 and 41 are located within 1° of each other. We

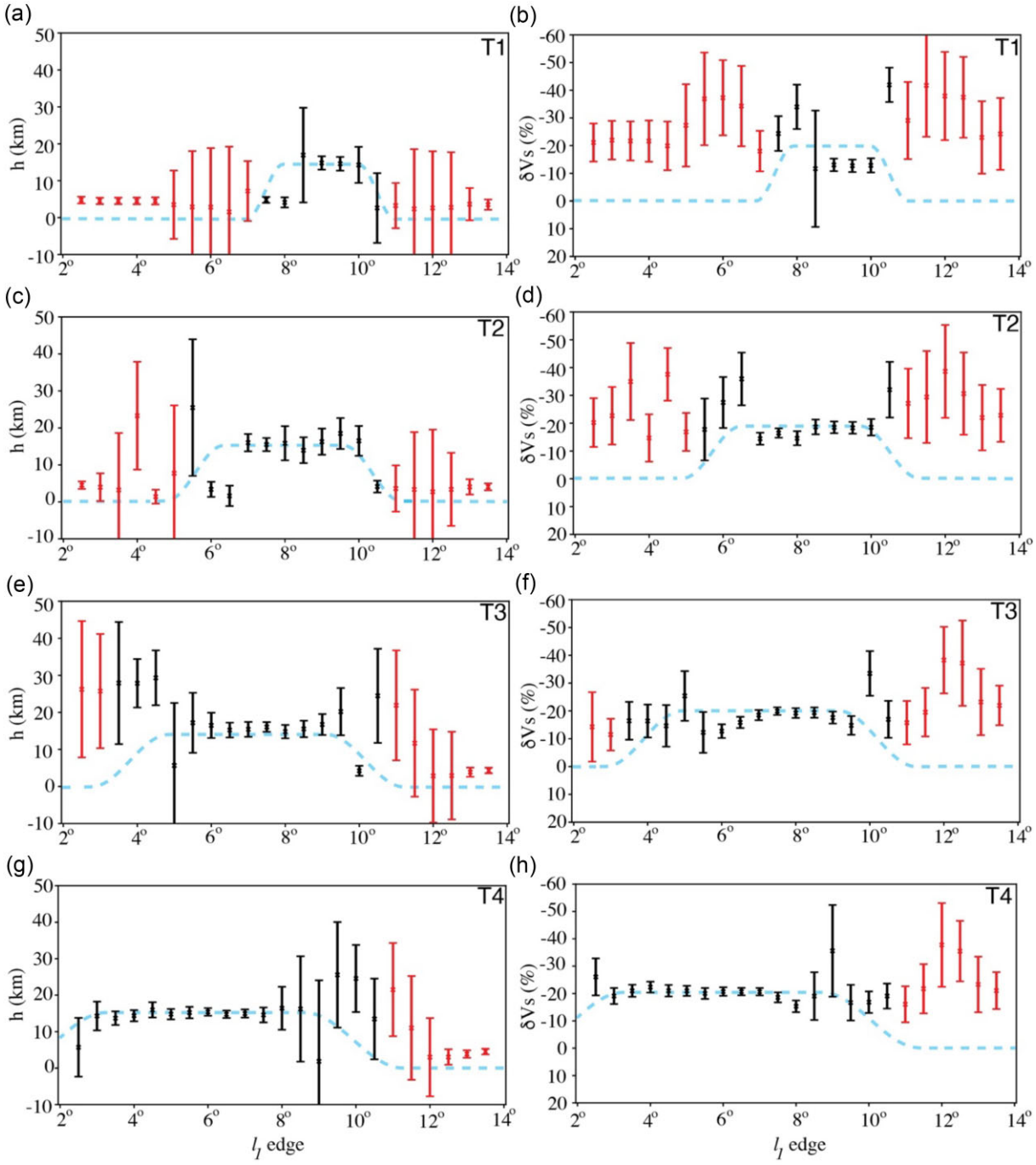

Figure 16. (a, c, e, g) Thickness (h) and (b, d, f, h) S-wave velocity perturbation (δVs) with their uncertainty (2-standard deviation) retrieved from the inversion of 2.5-D synthetic seismograms prepared for two Tukey shape models with various edge locations presented in Table 1 using full noise covariance matrix in the inversion. The blue dashed lines represent the true values. The edge locations along the x-axis in all subplots represent the average over three consecutive edge locations.

invert ScP waveforms from all events in each bin jointly including the attenuation parameter ($t*$) as an unknown parameter (Pachhai *et al.* 2023).

We first apply both approaches to a single ScP waveform from bin 37 (i.e. 0-th waveform in Fig. 20a) and compare this to the joint inversion using all events for this bin. When using real data, the noise covariance matrix is initially unknown. Therefore, we proceeded by first performing the inversion assuming that noise is uncorrelated, therefore, parametrizing the data noise using the standard deviation of noise (see eq. 6) (i.e. the noise standard deviation is also sampled as additional parameter). After convergence, we extract the maximum-likelihood model. The difference between the maximum-likelihood model prediction and observed data is considered as data noise and is used to compute the noise covariance matrix using eq. 10. This covariance matrix is then used in the second iteration of the inversion. Figs 21(a) and (b) shows the in-

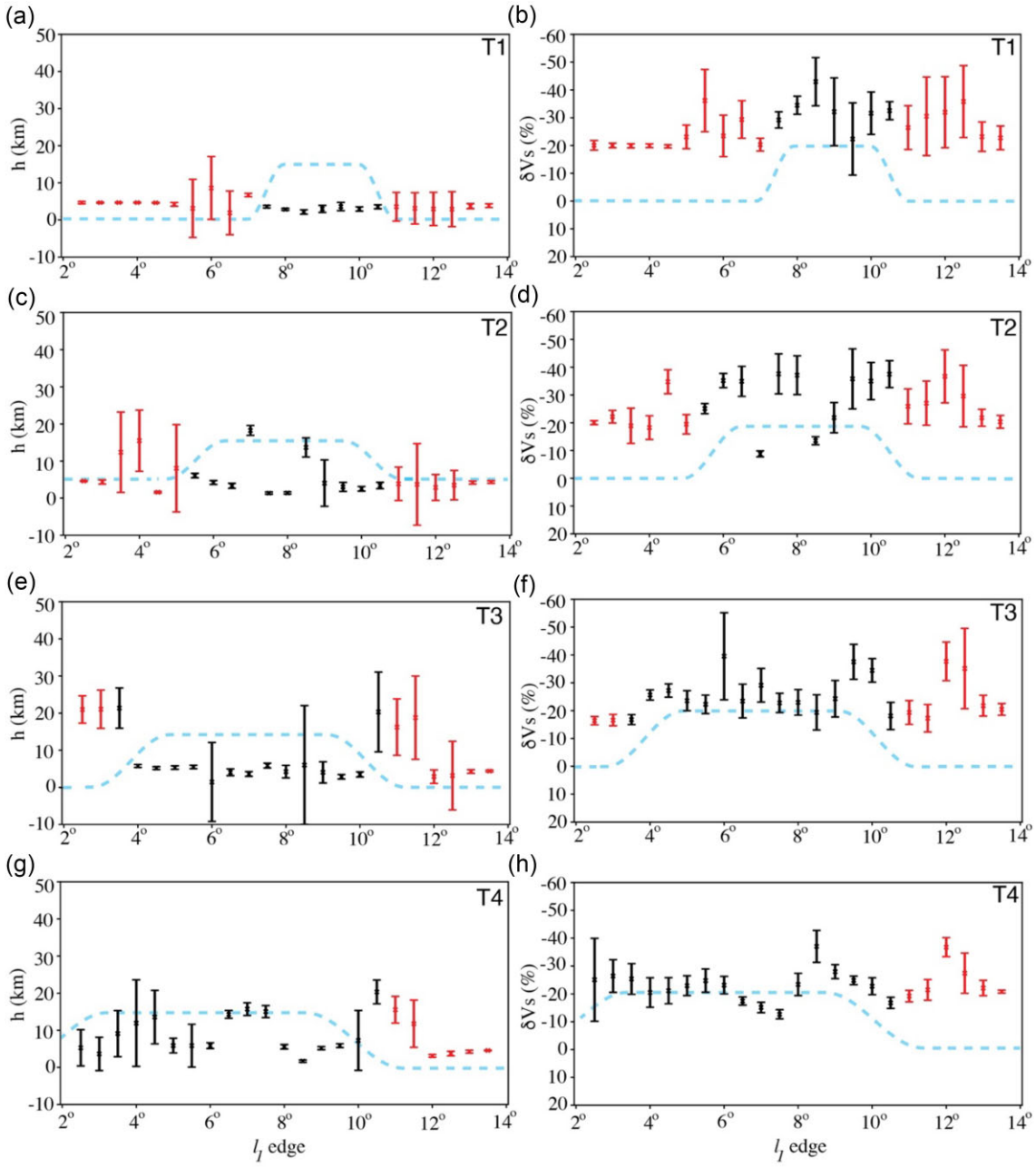

Figure 17. Same as Fig. 16, but the inversion was run using the covariance matrix computed for the residuals between 2.5-D ULVZ predictions and predictions for the maximum likelihood model.

version results when the AR1 model and covariance matrix methods are used, respectively. The inversion results are also summarized in Table 2. The inversion results for all the parameters are different other than that for δVs. Even for δVs, the uncertainties are larger when we consider the noise covariance matrix in the inversion. For other parameters, not only the uncertainties are large but also the parameter values are different (Table 2 and Fig. 21). For example, the ULVZ interface height and density are overestimated when AR1 parametrization is considered compared to that using a noise covariance matrix when we consider a single event (Table 2 and Figs 21a and b).

We then applied both approaches to all the ScP waveforms within bin 37 (see Fig. 20a for waveforms), and inversion results are shown in Figs 21(c) and (d). In the case of AR1 inversion, not only do the uncertainties become narrower but also the ULVZ parameters are close to that using covariance matrix in the inversion of a ScP waveform from a single event (Table 2 and Fig. 21). In contrast, the ULVZ parameters are not significantly different when considering 1 event or 14 events simultaneously in the case when the full data noise covariance matrix is considered in the inversion. Of course, the uncertainties become lower as we add more ScP waveforms from 14 events. This is because we have more data information to constrain the same ULVZ structure.

We also applied the same approach for ScP waveforms from two other bins. Inversion results for those bins are shown in Fig. 22. In the case of Bin 24, the inversion results do not change significantly

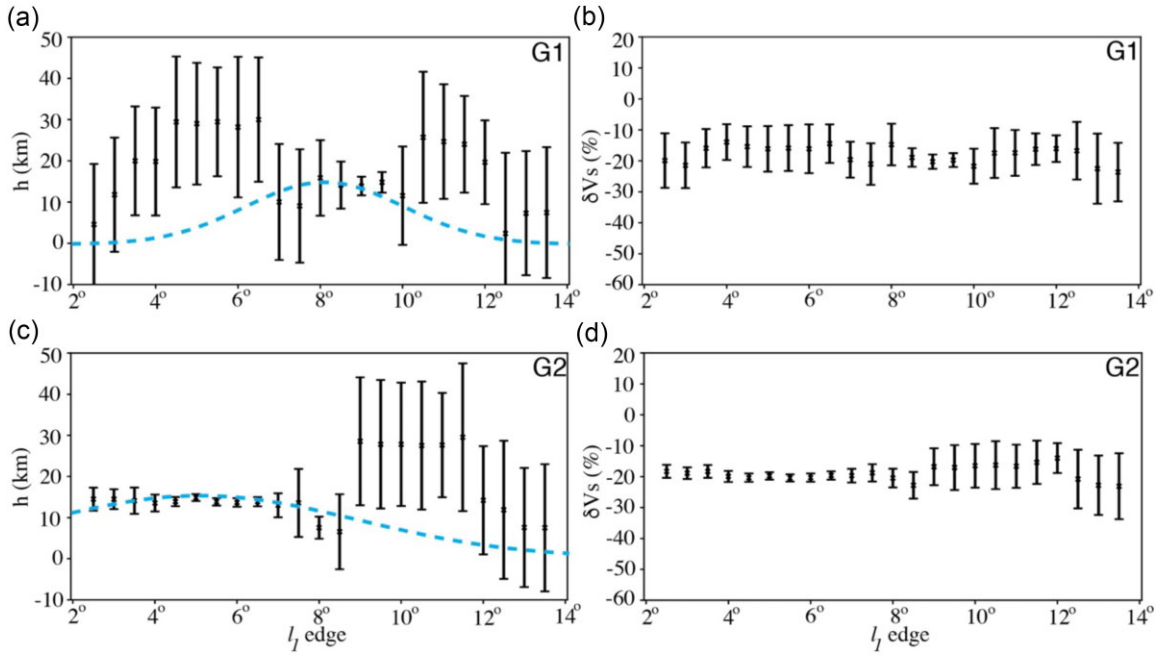

Figure 18. (a, c) Thickness (h) and (b, d) S-wave velocity perturbation (δVs) with their uncertainty (2-standard deviation) retrieved from the inversion of 2.5-D synthetic seismograms prepared for two Gaussian models with various edge locations presented in Table 1 using full noise covariance matrix in the inversion. The horizontal lines represent the true values. The edge locations along the x-axis in all subplots represent the average over three consecutive edge locations.

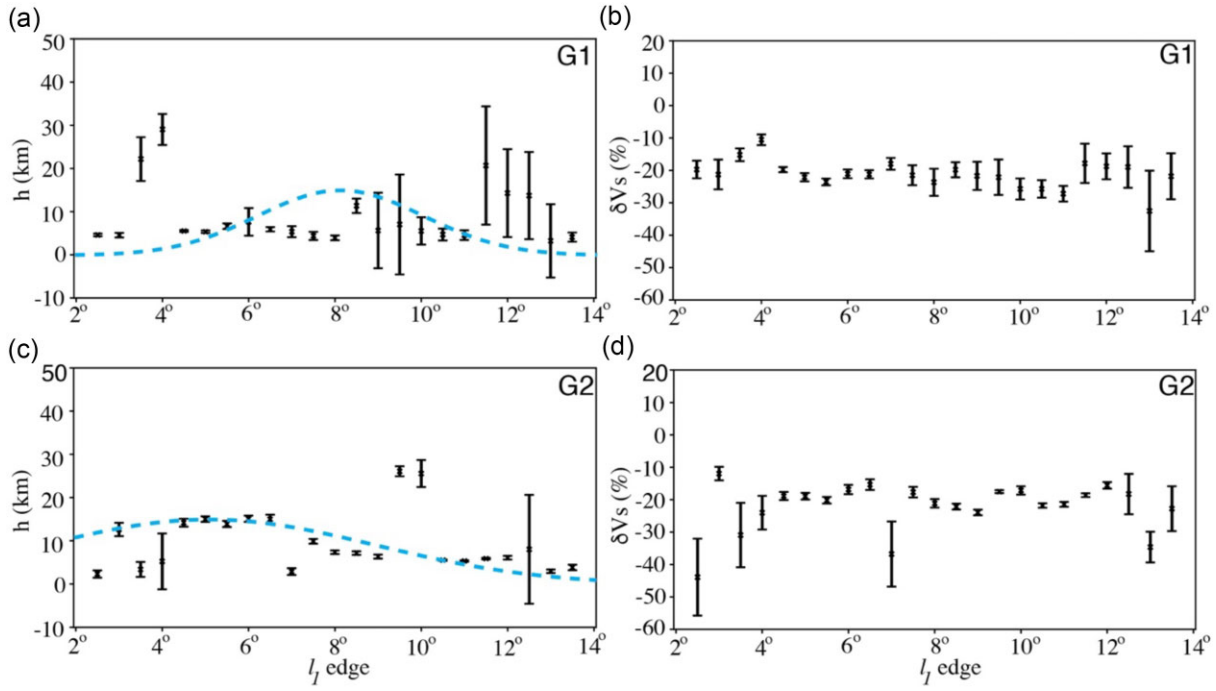

Figure 19. Same as Fig. 18, but the inversion was run using the covariance matrix computed for the residuals between 2.5-D ULVZ predictions and predictions for the maximum-likelihood model obtained from the first inversion. The first inversion was run using the covariance matrix computed for the residuals between 2.5-D ULVZ predictions and predictions for AK135 model. The blue dashed lines represent the true shape Gaussian ULVZs.

between two inversions other than uncertainties, but in the case of Bin 41, not only the parameter uncertainties are small but also the multiple modes appear when we consider AR1 parametrization of noise. When we consider the noise covariance matrix in the inversion, inversion retrieves a single model, which is one of the models in the inversion with AR1 parametrization of noise.

7 DISCUSSION AND CONCLUSIONS

This study addresses some of the challenges inherent in waveform modelling deep mantle seismic arrivals, particularly in terms of the effect of 2.5-D ULVZ shape and morphology on ScP waveforms. From the 2.5-D synthetic ScP waveforms, we found two arrivals emerging from the edges of the ULVZ (Sl_1P and Sl_2P). In many

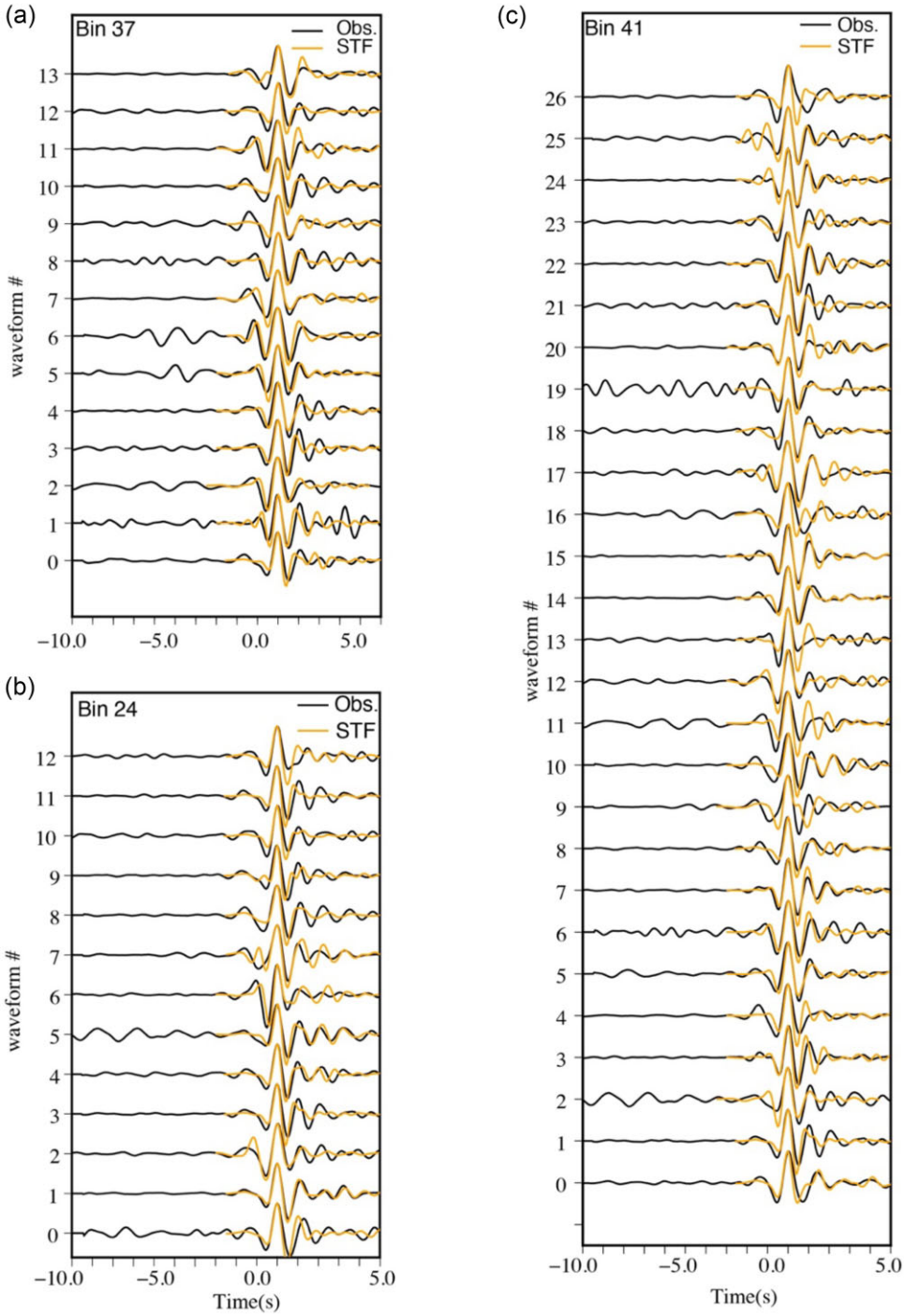

Figure 20. ScP waveforms considered as observed data (black lines) and *P* waveforms represented as STF (orange lines) waveforms from three different bins at the CMB, represented by stars in Fig. 1(a). Each waveform represents the stack of observed data (ScP) or *P* waveforms (i.e. STF) recorded by all the stations in a seismic array in Australia for an individual earthquake.

cases, the amplitude of the Sl_2P arrival is larger than that for the ScsP post-cursor and can interfere with the ScP and ScsP phases and in some cases can be misidentified as ScsP. The interference caused by these additional arrivals can create errors in the estimated ULVZ properties using a 1-D forward modelling approach. Whether or not these additional post-cursors cause interference is primarily dependent on the location of the ULVZ boundaries, which is typically unknown. Additionally, the precursor energy, particularly coming from the top of the ULVZ is not present when the ScP wavefield only interferes with 2.5-D ULVZ without hitting the ULVZ. This can have no control over the δVp and $\delta\rho$ as these parameters are mostly constrained by precursors, but the thickness and δV_S can be different than the true ULVZ parameters. There is a chance that we can still retrieve correct ULVZ parameters, particularly for *S*-wave velocity and thickness if ScP hits the location of the ULVZ, but that also depends on the size and shape of the ULVZ as the

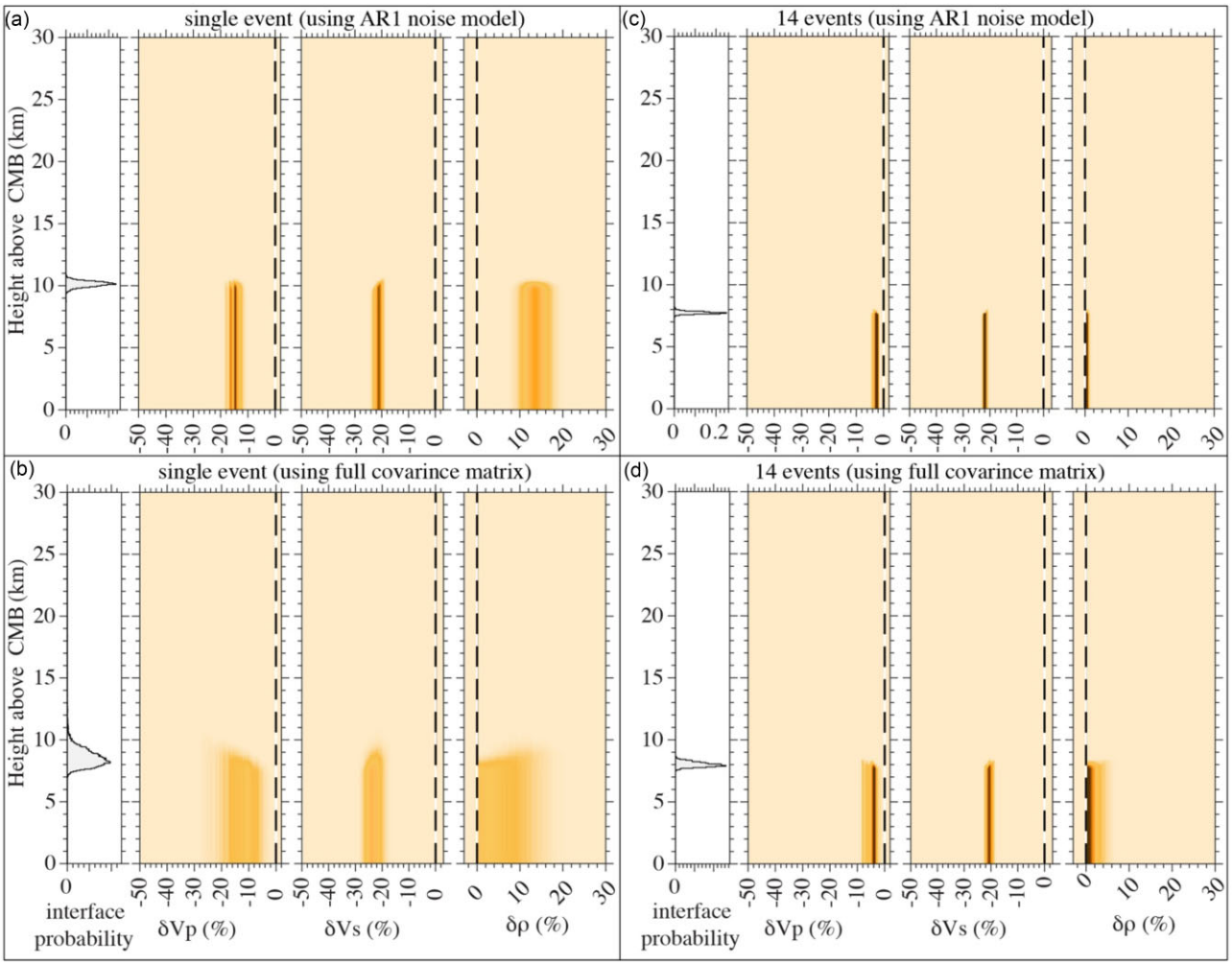

Figure 21. Posterior probability density of ULVZ height interface above the CMB, *P*-wave velocity (δVp), *S*-wave velocity (δVs) and density ($\delta\rho$) perturbations as a function of ULVZ height when a ScP waveform from a single event is used (a) assuming AR1 noise model (b) assuming full noise covariance matrix in the likelihood. (c) and (d) Same as in boxes (a) and (b) but for ScP waveforms from 14 events from Bin 37 in Fig. 1(a).

Table 2. ULVZ parameters with 2 standard deviations retrieved from the inversion of ScP waveforms from a single event and 14 events using AR1 noise model and full noise covariance matrix in the inversion in the case of bin 37.

	$h \pm$ 2std (km)	$\delta Vs \pm$ 2std (per cent)	$\delta Vp \pm$ 2std (per cent)	$\delta\rho \pm$ 2std (per cent)
1 event (using AR1 noise model)	10.2 ± 0.5	-21.2 ± 2.0	-14.7 ± 2.6	13.4 ± 4.0
1 event (using covariance matrix)	8.1 ± 1.4	-23.5 ± 4.0	-7.7 ± 9.6	0.4 ± 8.8
14 events (using AR1 noise model)	7.9 ± 0.2	-21.6 ± 0.8	-2.72 ± 0.9	0.1 ± 0.2
14 events (using covariance matrix)	8.0 ± 0.4	-20.8 ± 1.6	-3.8 ± 3.0	0.2 ± 2.4

ScsP post-cursor can constructively/destructively interfere with the phases coming from the edges (Figs 3–7).

To better understand these effects, we further developed a non-linear Bayesian inversion approach for ULVZ structure from ScP waveforms so that correlated data errors are fully accounted through the likelihood function (eq. 5). Past ULVZ studies developed the Bayesian inversion approximating the noise covariance matrix through the AR1 model for a single event (Pachhai *et al.* 2014, 2015) and multiple events (Pachhai *et al.* 2023). In the AR1 model, the autocovariance decays exponentially on two sides from the diagonal element (Fig. 8). However, we note that the retrieved parameter uncertainties depend strongly on the noise model. For example, the Boxcar model shows well pronounced energy coming from the right edge of ULVZ which can be mis-identified as ScsP if we just use the AR1 noise model, thereby providing unrealistically high confidence on the estimated ULVZ parameters constrained by that post-cursor (e.g. Figs 11–12 and Figs S1–S6). It can also overestimate the *S*-wave velocity perturbation and the density and *P*-wave velocity perturbation with narrow uncertainties when we consider 1-D forward computation in the inversion. When we use the full noise covariance matrix in the inversion, the uncertainties become larger, but those inversions also do not recover true values in some cases, particularly when 1-D prediction can explain some of the post-cursor like features resulting from the interaction of ScP with the edges of the boxcar ULVZ. This effect is even more evident when we consider the iterative approach as the inversion tries to fit

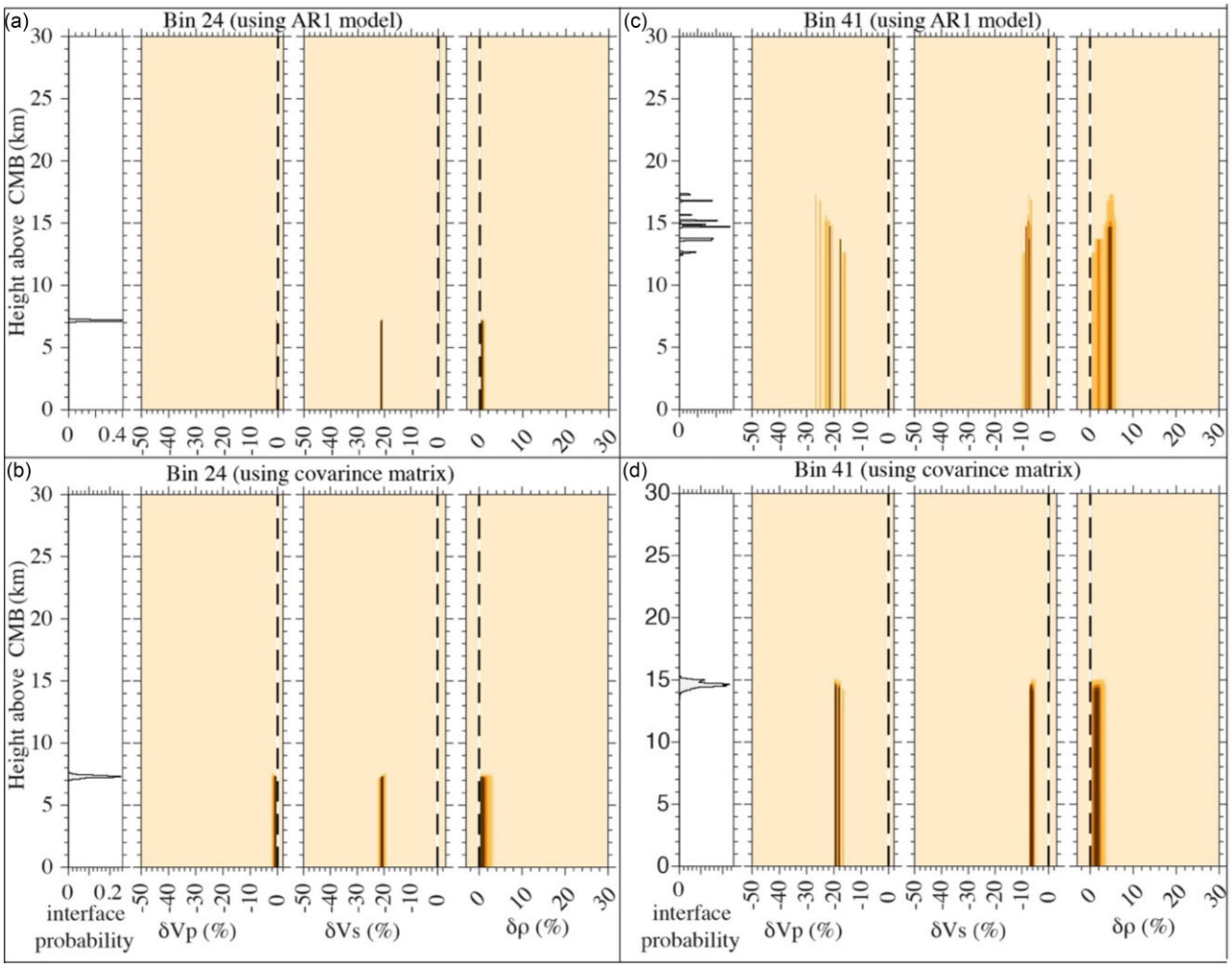

Figure 22. Posterior probability density of ULVZ height interface above the CMB, *P*-wave velocity (δVp), *S*-wave velocity (δVs) and density ($\delta\rho$) perturbations as a function of ULVZ height when all the ScP waveform from Bin 24, in Fig. 1(a), are used (a) assuming AR1 noise model (b) assuming full noise covariance matrix in the likelihood. (c) and (d) Same as in boxes (a) and (b) but for Bin 41 in Fig. 1(a).

1-D like signals using 1-D forward computation thereby overestimating/underestimating the ULVZ parameters depending on where the ScP strikes the ULVZs and where the ULVZ edges are located. However, these effects are minimal when we consider longer ULVZ and smoother edges, for example, Tukey and Gaussian ULVZs.

An important point of this paper is that reliable estimation of the PPD of the ULVZ parameters requires the specification of a physically meaningful likelihood function. The error correlations must be quantified and included in the inversion employing data covariance matrices. Inversion of 2.5-D synthetics show that the ULVZ parameters are recovered close to the true parameters with wider, more realistic, uncertainties when we consider the data noise covariance matrix. But there are still a couple of cases when the ULVZ parameters are not well recovered. The first case is when the noise is non-stationary. This means that the standard deviation and correlation of noise changes as a function of time which is possible when analysing real data. Here we assume that the noise is stationary, which we think is fair in the short time windows we are examining. To account for non-stationary noise, we could consider scaling the autocovariance as a function of moving windows. The second case is when the Sl_1P and Sl_2P arrivals interfere constructively or destructively with the ScsP phase. In some cases, these arrivals make it appear that ScsP has a much larger amplitude which is not captured by the covariance matrix. Our inclusion of multiple events helps us to reduce the overestimation of ULVZ parameters in this case, but we cannot fully eliminate this problem using only 1-D forward modelling approaches, and it is not yet computationally feasible to use 2.5-D methods in the Bayesian approach.

When applying our technique to real data, the covariance matrix can become non-positive definite resulting in a non-invertible matrix. To make the covariance matrix invertible, we apply weak damping when necessary. Unlike the synthetic data, with real data the noise covariance matrix is unknown. In this case we apply an iterative approach, where at each iteration we calculate the covariance matrix from the residuals between the observed data and the maximum-likelihood model prediction. This process is repeated until we find the same covariance matrix in consecutive iterations. We found that 2 to 3 iterations are enough for the convergence of the covariance matrix. Additionally, the inversion of ULVZ parameters is more efficient when we consider the covariance matrix in the likelihood, which is especially helpful for the geographic bins with a large number of events (e.g. bin 41 considered in this study). This is because the previous inversion (e.g. Pachhai *et al.* 2023) samples two additional parameters for the AR1 noise model for each waveform. Including these two additional parameters, for each waveform, significantly increases the number of parameters and the

time to convergence. As the inversion did not converge even after running for weeks, Pachhai *et al.* (2023) fixed the $t*$ values based on the inversion of ScP waveform from individual events. Using this approach, we retrieved PREM-like ULVZ parameters and the majority of waveforms in this bin do not have well pronounced ScP pre- and post-cursors. Fig. 22(c) also shows multiple modes for thickness as the inversion is not yet converged. But when we use the covariance matrix approach, the inversion converges and show a unique solution with $h = 15$ km, $\delta Vs = \sim$-7 per cent, and $\delta Vp = \sim$-20 per cent, still suggesting weak ULVZ but the δVp is unusually large compared to δVs. These controversial results may be because ScP is hitting near a 2-D/3-D ULVZ edge location, thereby providing phases that are not present in the 1-D modelling, but the inversion is trying to fit those phases differently when different approaches are considered.

Past studies have also identified ScP waveforms that show ULVZ-like behaviour with large amplitude post-cursors in the absence of precursors. For example, Garnero & Vidale (1999) show both presence and absence of ScP precursors that sample the CMB beneath the Central Pacific region. Similarly, Persh *et al.* (2001) presented ScP observations without precursors that sample the CMB beneath Central America and Mexico. Past studies have reported ScP post-cursors without any precursors in our study region as well (e.g. Rost & Revenaugh 2003; Rost *et al.* 2005). More recently, Idehara *et al.* (2007) found ScP data without precursors that sample the CMB beneath the east of Australia, and Pachhai *et al.* (2023) also found events without precursors. Hence, the ULVZ literature shows several examples where our findings in this study are relevant. Namely, the existence of ScP post-cursors without accompanying precursors appears quite common and is possibly linked to ScP arrivals that do not directly strike the ULVZ. Parameters recovered in such cases must be treated with caution. Moreover, Pachhai *et al.* (2023) presented evidence for an additional large amplitude signal several seconds after the ScsP post-cursor. This extra arrival is consistent with additional post-cursor energy generated from ULVZ boundaries (Sl_1P and Sl_2P) and may be indicative of the finite size of the ULVZ beneath the Coral Sea, however, more in-depth investigation is needed for such confirmation.

In conclusion, 2.5-D synthetic waveforms show additional waveform complexity resulting from the edges of the ULVZs which can interfere with the converted phases of ScP. As a result, the estimation of ULVZ properties using the 1-D forward modelling can provide misleading ULVZ parameter values, which can lead to the improper physical origin of ULVZs. The Bayesian inversion of ScP waveforms can constrain ULVZ parameters correctly if the data noise is correctly addressed. From the inversion of synthetic data, we found that the inversion recovers ULVZ parameters well with wider, more realistic, uncertainties if we know the full covariance matrix and include it in the inversion, but addressing data noise through the AR1 model can recover ULVZ parameter values far from the true values with unrealistically high confidence. This suggests that making a decision just based on the narrowness of the uncertainties can lead to misinterpretation. Inversion for the observed data also shows wider uncertainties for all the ULVZ parameters if we consider the noise covariance matrix in the inversion. Additionally, the ULVZ parameters can also be different depending on what noise model we consider in the inversion. We believe that the inclusion of the noise covariance matrix performs better than the AR1 model because that provides more consistent results between the inversion of ScP waveforms from both single event and multiple events. Our synthetic experiments demonstrate that we can recover ULVZ parameters accurately for a wide variety of models if the noise covariance matrix is known, even when using a 1-D forward modelling approach in the inversion. But when the covariance matrix is unknown and inversion is performed iteratively, we can recover still recover ULVZ shape and properties when the ULVZ is large. Our confidence in the procedure is significantly enhanced when SPcP precursors are also identifiable in the waveforms, which indicates we are directly striking the ULVZ. Application of these techniques to data collected for ScP waveforms sampling the Coral Sea region recover ULVZ parameters with $\delta Vs = -20.8 \pm 0.8$ per cent and $h = 8 \pm 0.2$ km in the case of bin 37 and $\delta Vs = -21.7 \pm 0.8$ per cent and $h = 7.3 \pm 0.2$ km in the case of bin 24. These values are determined using multiple inversion techniques and are here vetted against possible 2-D ULVZ structural complications. The systematic application of this approach will allow us to provide better estimates of ULVZ geometrical and elastic parameters and their proper physical interpretation.

ACKNOWLEDGMENTS

SP would like to thank Jan Dettmer for insightful discussion about the inversion method. We would also like to thank the editor Ebru Bozdag and Satoru Tanaka for providing feedback that improved the manuscript. We acknowledge the University of Utah Center for High Performance Computing (CHPC) for computing resources and support. MT and SP were partially funded by National Science Foundation (NSF) grant EAR 2341237.

SUPPORTING INFORMATION

Supplementary data are available at *GJIRAS* online.

Figure S1. (a) Thickness and (b) *S*-wave velocity perturbation (δVs) with their uncertainty (2-standard deviations) retrieved from the inversion, using the AR1 model in the likelihood function (eq. 9), of 2-D synthetic seismograms prepared for the Boxcar model of various widths and edge locations presented in Table 1. (c) and (d) same as (a) and (b) but using the full data noise covariance matrix in the likelihood function (eq. 5). The horizontal lines represent the true values. In these inversions a single waveform was used.

Figure S2. (a) *P*-wave velocity perturbation (δVp) and (b) density perturbation ($\delta\rho$) with their uncertainty (2-standard deviations) retrieved from the inversion, using AR1 model in the likelihood function (eq. 9), of 2-D synthetic seismograms prepared for the Boxcar model of various widths and edge locations presented in Table 1. (c) and (d) same as (a) and (b) but using the full data noise covariance matrix in the likelihood function (eq. 5). The horizontal lines represent the true values. In these inversions a single waveform was used.

Figure S3. (a) Thickness and (b) *S*-wave velocity perturbation (δVs) with their uncertainty (2-standard deviations) retrieved from the inversion, using the AR1 model in the likelihood function (eq. 9), of 2-D synthetic seismograms prepared for the Tukey model of various widths and edge locations presented in Table 1. (c) and (d) same as (a) and (b) but using the full data noise covariance matrix in the likelihood function (Eq. 5). The horizontal lines represent the true values. In these inversions a single waveform was used.

Figure S4. (a) *P*-wave velocity perturbation (δVp) and (b) density perturbation ($\delta\rho$) with their uncertainty (2-standard deviations) retrieved from the inversion, using the AR1 model in the likelihood function (eq. 9), of 2-D synthetic seismograms prepared for the Tukey model of various widths and edge locations presented in Table 1. (c) and (d) same as (a) and (b) but using the full data noise

covariance matrix in the likelihood function (eq. 5). The horizontal lines represent the true values. In these inversions a single waveform was used.

Figure S5. (a) Thickness and (b) *S*-wave velocity perturbation (δVs) with their uncertainty (2-standard deviations) retrieved from the inversion, using the AR1 model in the likelihood function (eq. 9), of 2-D synthetic seismograms prepared for the Gaussian model of various widths and edge locations presented in Table 1. (c) and (d) same as (a) and (b) but using the full data noise covariance matrix in the likelihood function (eq. 5). The horizontal lines represent the true values. In these inversions a single waveform was used.

Figure S6. (a) *P*-wave velocity perturbation (δVp) and (b) with their uncertainty (2-standard deviations) retrieved from the inversion, using the AR1 model in the likelihood function (eq. 9), of 2-D synthetic seismograms prepared for the Gaussian model of various widths and edge locations presented in Table 1. (c) and (d) same as (a) and (b) but using the full data noise covariance matrix in the likelihood function (eq. 5). The horizontal lines represent the true values. In these inversions a single waveform was used.

Figure S7. (a, c, e, g) Density perturbation ($\delta\rho$) (h) and (b, d, f, h) *P*-wave velocity perturbation (δVp) with their uncertainty (2-standard deviations) retrieved from the inversion of 2.5-D synthetic seismograms prepared for four boxcar models of various widths and edge locations presented in Table 1 using the full noise covariance matrix in the inversion. The edge locations along the x-axis in all subplots represent the average over three consecutive edge locations. The light blue dashed lines represent the true values of ULVZ parameters and vertical dashed lines indicate the l_1 edge boundaries within which ScP strikes the ULVZ. The black error bars represent the ULVZ parameters recovered within a line where ScP hits the ULVZ while the red color error bars represent the ULVZ parameters recovered from the line where ScP does not directly hit the ULVZ including edges.

Figure S8. Same as Fig. S7, but the inversion was run using the covariance matrix computed for the residuals between 2.5-D ULVZ predictions and predictions for the maximum likelihood model obtained from the first inversion. The first inversion was run using the full covariance matrix computed for the residuals between 2.5-D ULVZ predictions and predictions for AK135 model.

Figure S9. (a, c, e, g) Density perturbation ($\delta\rho$) (h) and (b, d, f, h) *P*-wave velocity perturbation (δVp) with their uncertainty (2-standard deviations) retrieved from the inversion of 2.5-D synthetic seismograms prepared for four Tukey window models of various width and edge locations presented in Table 1 using full noise covariance matrix in the inversion. The edge locations along the x-axis in all subplots represent the average over three consecutive edge locations. The light blue dashed lines represent the true values of ULVZ parameters and vertical dashed lines indicate the l_1 edge boundaries within which ScP strikes the ULVZ. The black error bars represent the ULVZ parameters recovered within a line where ScP hits the ULVZ while the red colour error bars represent the ULVZ parameters recovered from the line where ScP does not directly hit the ULVZ including edges.

Figure S10. Same as Fig. S9, but the inversion was run using the covariance matrix computed for the residuals between 2.5-D ULVZ predictions and predictions for the maximum likelihood model obtained from the first inversion. The first inversion was run using the covariance matrix computed for the residuals between 2.5-D ULVZ predictions and predictions for AK135 model.

Figure S11. (a, c) Density ($\delta\rho$) and (b, d) *S*-wave velocity perturbation (δVp) with their uncertainty (2-standard deviations) retrieved from the inversion of 2.5-D synthetic seismograms prepared for two Gaussian models with various edge locations presented in Table 1 using full noise covariance matrix in the inversion. The edge locations along the x-axis in all subplots represent the average over three consecutive edge locations. The true values for $\delta\rho$ and δVp are 5 per cent and -10 per cent, respectively.

Figure S12. Same as Fig. S11, but the inversion was run using the covariance matrix computed for the residuals between 2.5-D ULVZ predictions and predictions for the maximum likelihood model obtained from the first inversion. The first inversion was run using the covariance matrix computed for the residuals between 2.5-D ULVZ predictions and predictions for AK135 model. The true values for density and δVp are 5 per cent and -10 per cent, respectively.

Please note: Oxford University Press are not responsible for the content or functionality of any supporting materials supplied by the authors. Any queries (other than missing material) should be directed to the corresponding author for the article.

DATA AVAILABILITY

We used ScP waveforms from Pachhai *et al.* (2023) that are publicly available through uhive (https://hive.utah.edu), University of Utah Research Data Repository: https://doi.org/10.7278/S50d-a67s-y717. The facilities of IRIS Data Services, and specifically the IRIS Data Management Center, were used to access the raw waveforms that are processed and stored in uhive, related metadata and/or derived products used in this study. IRIS Data Services are funded through the Seismological Facilities for the Advancement of Geoscience and EarthScope (SAGE) Proposal for the National Science Foundation under Cooperative Agreement EAR-1261681. The Bayesian inversion algorithm applied in this paper is available from https://zenodo.org/records/7825575 (Pachhai 2023).

REFERENCES

Andrault, D., Pesce, G., Bouhifd, M.A., Bolfan-Casanova, N., Hénot, J.-M. & Mezouar, M., 2014. Melting of subducted basalt at the core-mantle boundary, *Science,* **344,** 892–895.

Brown, S.P., Thorne, M.S., Miyagi, L. & Rost, S., 2015. A compositional origin to ultralow-velocity zones, *Geophys. Res. Lett.,* **42,** 1039–1045.

Chapman, C. & Orcutt, J., 1985. The computation of body wave synthetic seismograms in laterally homogeneous media, *Rev. Geophys.,* **23,** 105–163.

Cottaar, S., Martin, C., Li, Z. & Parai, R., 2022. The root to the Galápagos mantle plume on the core-mantle boundary, *Seismica,* **1**(1), 1–12, doi: 10.26443/seismica.v1i1.197.

Cottaar, S. & Romanowicz, B., 2012. An unsually large ULVZ at the base of the mantle near Hawaii, *Earth planet. Sci. Lett.,* **355-356,** 213–222.

Dettmer, J. & Dosso, S.E., 2012. Trans-dimensional matched-field geoacoustic inversion with hierarchical error models and interacting Markov chains, *J. acoust. Soc. Am.,* **132,** 2239–2250.

Dettmer, J., Dosso, S.E. & Holland, C.W., 2007. Uncertainty estimation in seismo-acoustic reflection travel time inversion, *J. acoust. Soc. Am.,* **122,** 161–176.

Dziewonski, A.M. & Anderson, D.L., 1981. Preliminary reference Earth model, *Phys. Earth planet. Inter.,* **25,** 297–356.

Garnero, E.J., Grand, S.P. & Helmberger, D.V., 1993. Low *P*-wave velocity at the base of the mantle, *Geophys. Res. Lett.,* **20,** 1843–1846.

Garnero, E.J. & Helmberger, D.V., 1995. A very slow basal layer underlying large-scale low-velocity anomalies in the lower mantle beneath the Pacific: evidence from core phases, *Phys. Earth planet. Inter.,* **91,** 161–176.

Garnero, E.J. & Helmberger, D.V., 1996. Seismic detection of a thin laterally varying boundary layer at the base of the mantle beneath the central-Pacific, *Geophys. Res. Lett.,* **23,** 977–980.

Garnero, E.J. & Helmberger, D.V., 1998. Further structural constraints and uncertainties of a thin laterally varying ultralow-velocity layer at the base of the mantle, *J. geophys. Res.,* **103,** 12 495–12 509.

Garnero, E.J. & Vidale, J.E., 1999. ScP; a probe of ultralow velocity zones at the base of the mantle, *Geophys. Res. Lett.,* **26,** 377–380.

Gilks, W.R. & Roberts, G.O., 1996. Strategies for improving MCMC, in *Markov Chain Monte Carlo in Practice, Vol. 6,* 89–114, eds Gilks, W.R., Richardson, S. & Spiegelhalter, D., Chapman and Hall.

Havens, E. & Revenaugh, J., 2001. A broadband seismic study of the lowermost mantle beneath Mexico: constraints on ultralow velocity zone elasticity and density, *J. geophys. Res.: Solid Earth,* **106,** 30 809–30 820.

Helmberger, D.V., Wen, L. & Ding, X., 1998. Seismic evidence that the source of the Iceland hotspot lies at the core-mantle boundary, *Nature,* **396,** 251–255.

Idehara, K., 2011. Structural heterogeneity of an ultra-low-velocity zone beneath the Philippine Islands: implications for core–mantle chemical interactions induced by massive partial melting at the bottom of the mantle, *Phys. Earth planet. Inter.,* **184,** 80–90.

Idehara, K., Yamada, A. & Zhao, D., 2007. Seismological constraints on the ultralow velocity zones in the lowermost mantle from core-reflected waves, *Phys. Earth planet. Inter.,* **165,** 25–46.

Jahnke, G., 2009. Methods for seismic wave propagation on local and global scales with finite differences, Dissertation, LMU, Mu¨nchen: Fakultät fu¨r Geowissenschaften.

Jenkins, J., Mousavi, S., Li, Z. & Cottaar, S., 2021. A high-resolution map of Hawaiian ULVZ morphology from ScS phases, *Earth planet. Sci. Lett.,* **563,** 1–13.

Jensen, K.J., Thorne, M.S. & Rost, S., 2013. SPdKS analysis of ultralow-velocity zones beneath the western Pacific, *Geophys. Res. Lett.,* **40,** 4574–4578.

Kanda, R.V. & Stevenson, D.J., 2006. Suction mechanism for iron entrainment into the lower mantle, *Geophys. Res. Lett.,* **33,** 1–4, doi: 10.1029/2005GL025009.

Kennett, B.L., Engdahl, E. & Buland, R., 1995. Constraints on seismic velocities in the Earth from traveltimes, *Geophys. J. Int.,* **122,** 108–124.

Komatitsch, D. & Tromp, J., 2002. Spectral-element simulations of global seismic wave propagation—I. Validation, *Geophys. J. Int.,* **149,** 390–412.

Koper, K.D. & Pyle, M.L., 2004. Observations of PKiKP/PcP amplitude ratios and implications for Earth structure at the boundaries of the liquid core, *J. geophys. Res.: Solid Earth,* **109,** B03301, doi:.

Krier, J., Thorne, M.S., Leng, K. & Nissen-Meyer, T., 2021. A compositional component to the Samoa ultralow-velocity zone revealed through 2-and 3-D waveform modeling of SKS and SKKS differential traveltimes and amplitudes, *J. geophys. Res.: Solid Earth,* **126,** 1–20, doi: 10.1029/2021JB021897.

Labrosse, S., Hernlund, J. & Coltice, N., 2007. A crystallizing dense magma ocean at the base of the Earth's mantle, *Nature,* **450,** 866–869.

Leng, K., Korenaga, J. & Nissen-Meyer, T., 2020. 3-D scattering of elastic waves by small-scale heterogeneities in the Earth's mantle, *Geophys. J. Int.,* **223,** 502–525.

Leng, K., Nissen-Meyer, T. & van Driel, M., 2016. Efficient global wave propagation adapted to 3-D structural complexity: a pseudospectral/spectral-element approach, *Geophys. Suppl. Mon. Not. R. astr. Soc.,* **207,** 1700–1721.

Li, M., McNamara, A.K., Garnero, E.J. & Yu, S., 2017. Compositionally-distinct ultra-low velocity zones on Earth's core-mantle boundary, *Nat. Commun.,* **8,** 1–9.

Li, Y., Deschamps, F. & Tackley, J.P., 2016. Small post-perovskite patches at the base of lower mantle primordial reservoirs: insights from 2-D numerical modeling and implications for ULVZs, *Geophys. Res. Lett.,* **43,** 3215–3225.

Mao, W.L. *et al.* 2006. Iron-rich post-perovskite and the origin of ultralow-velocity zones, *Science,* **312,** 564–565.

McNamara, A.K., 2019. A review of large low shear velocity provinces and ultra low velocity zones, *Tectonophysics,* **760,** 199–220.

McNamara, A.K., Garnero, E.J. & Rost, S., 2010. Tracking deep mantle reservoirs with ultra-low velocity zones, *Earth planet. Sci. Lett.,* **299,** 1–9.

Mori, J. & Helmberger, D.V., 1995. Localized boundary layer below the mid-Pacific velocity anomaly identified from a PcP precursor, *J. geophys. Res.: Solid Earth,* **100,** 20 359–20 365.

Pachhai, S., 2023. Transdimensional hierarchical Bayesian inversion of phase and group velocity, Zenodo, https://zenodo.org/records/7825575 (Date of deposit is April 13, 2023).

Pachhai, S., Dettmer, J. & Tkalčić, H., 2015. Ultra-low velocity zones beneath the Philippine and Tasman Seas revealed by a trans-dimensional bayesian waveform inversion, *Geophys. J. Int.,* **203,** 1302–1318.

Pachhai, S., Li, M., Thorne, M.S., Dettmer, J. & Tkalčić, H., 2022. Internal structure of ultralow-velocity zones consistent with origin from a basal magma ocean, *Nat. Geosci.,* **15,** 79–84.

Pachhai, S., Thorne, M.S. & Rost, S., 2023. Improved characterization of ultralow-velocity zones through advances in bayesian inversion of ScP waveforms, *J. geophys. Res.: Solid Earth,***128,** 1–27. doi: 10.1029/2023JB026415.

Pachhai, S., Tkalčić, H. & Dettmer, J., 2014. Bayesian inference for ultralow velocity zones in the Earth's lowermost mantle: complex ULVZ beneath the east of the Philippines, *J. geophys. Res.: Solid Earth,* **119,** 8346–8365.

Persh, S.E., Vidale, J.E. & Earle, P.S., 2001. Absence of short-period ULVZ precursors to PcP and ScP from two regions of the CMB, *Geophys. Res. Lett.,* **28,** 387–390.

Rawlinson, N. & Kennett, B.L., 2004. Rapid estimation of relative and absolute delay times across a network by adaptive stacking, *Geophys. J. Int.,* **157,** 332–340.

Reasoner, C. & Revenaugh, J., 2000. ScP constraints on ultralow-velocity zone density and gradient thickness beneath the Pacific, *J. geophys. Res.: Solid Earth,* **105,** 28 173–28 182.

Revenaugh, J. & Meyer, R., 1997. Seismic evidence of partial melt within a possibly ubiquitous low-velocity layer at the base of the mantle, *Science,* **277,** 670–673.

Rondenay, S., Cormier, V.F. & Van Ark, E.M., 2010. SKS and SPdKS sensitivity to two-dimensional ultralow-velocity zones, *J. geophys. Res.,* **115,** 1–17, doi: 10.1029/2009JB006733.

Rondenay, S. & Fischer, K.M., 2003. Constraints on localized core-mantle boundary structure from multichannel, broadband SKS coda analysis, *J. geophys. Res.: Solid Earth,* **108,** 1–16, doi: 10.1029/2003JB002518.

Rost, S., Garnero, E.J. & Stefan, W., 2010. Thin and intermittent ultralow-velocity zones, *J. geophys. Res.: Solid Earth,* **115,** 1–12, doi: 10.1029/2009JB006981.

Rost, S., Garnero, E.J. & Williams, Q., 2006. Fine-scale ultralow-velocity zone structure from high-frequency seismic array data, *J. geophys. Res.: Solid Earth,* **111,** 1–14, doi: 10.1029/2005JB004088.

Rost, S., Garnero, E.J., Williams, Q. & Manga, M., 2005. Seismological constraints on a possible plume root at the core–mantle boundary, *Nature,* **435,** 666–669.

Rost, S. & Revenaugh, J., 2001. Seismic detection of rigid zones at the top of the core, *Science,* **294,** 1911–1914.

Rost, S. & Revenaugh, J., 2003. Small-scale ultralow-velocity zone structure imaged by ScP, *J. geophys. Res.: Solid Earth,* **108,** 1–10, doi: 10.1029/2001JB001627.

Schwarz, B., 2019. An introduction to seismic diffraction, *Adv. Geophys.,* **60,** 1–64.

Sun, D., Helmberger, D., Lai, V., Gurnis, M., Jackson, J. & Yang, H.Y., 2019. Slab control on the northeastern edge of the mid-Pacific LLSVP near Hawaii, *Geophys. Res. Lett.,* **46,** 3142–3152.

Thorne, M.S. & Garnero, E.J., 2004. Inferences on ultralow-velocity zone structure from a global analysis of SPdKS waves, *J. geophys. Res.: Solid Earth,* **109,** 1–22, doi: 10.1029/2004JB003010.

Thorne, M.S., Garnero, E.J., Jahnke, G., Igel, H. & McNamara, A.K., 2013. Mega Ultra Low velocity zone and mantle flow, *Earth planet. Sci. Lett.,* **364,** 59–67.

Thorne, M.S., Pachhai, S., Leng, K., Wicks, J.K. & Nissen-Meyer, T., 2020. New candidate ultralow-velocity zone locations from highly anomalous SPdKS waveforms, *Minerals,* **10,** 1–26, doi: 10.3390/min10030211.

Thorne, M.S., Leng, K., Pachhai, S., Rost, S., Wicks, J. & Nissen-Meyer, T., 2021. The most parsimonious ultralow-velocity zone distribution from highly anomalous SPdKS waveforms, *Geochem. Geophys. Geosyst.,* **22,** 1–29, doi: 10.1029/2020GC009467.

Thybo, H., Ross, A.R. & Egorkin, A., 2003. Explosion seismic reflections from the Earth's core, *Earth planet. Sci. Lett.,* **216,** 693–702.

Vanacore, E.A., Rost, S. & Thorne, M.S., 2016. Ultralow-velocity zone geometries resolved by multidimensional waveform modeling, *Geophys. J. Int.,* **206,** 659–674.

Wen, L. & Helmberger, D.V., 1998. A two-dimensional P-SV hybrid method and its application to modeling localized structures near the core-mantle boundary, *J. geophys. Res.,* **103,** 17 901–17 918.

Wicks, J., Jackson, J. & Sturhahn, W., 2010. Very low sound velocities in iron-rich (Mg, Fe) O: implications for the core-mantle boundary region, *Geophys. Res. Lett.,* **37,** 1–5, doi: 10.1029/2010GL043689.

Williams, Q. & Garnero, E.J., 1996. Seismic evidence for partial melt at the base of Earth's mantle, *Science,* **273,** 1528–1530.

Williams, Q., Revenaugh, J. & Garnero, E., 1998. A correlation between ultra-low basal velocities in the mantle and hot spots, *Science,* **281,** 546–549.

Yu, S. & Garnero, E.J., 2018. Ultralow velocity zone locations: a global assessment, *Geochem. Geophys. Geosyst.,* **19,** 396–414.

Yuan, K. & Romanowicz, B., 2017. Seismic evidence for partial melting at the root of major hot spot plumes, *Science,* **357,** 393–397.